

Vortex shedding suppression in mixed convective flow past a square cylinder subjected to large-scale heating using a non-Boussinesq model

Cite as: Phys. Fluids **31**, 023602 (2019); <https://doi.org/10.1063/1.5079516>

Submitted: 31 October 2018 . Accepted: 09 January 2019 . Published Online: 04 February 2019

Md. Reyaz Arif , and Nadeem Hasan 



View Online



Export Citation



CrossMark

PHYSICS TODAY
WHITEPAPERS

ADVANCED LIGHT CURE ADHESIVES

Take a closer look at what these environmentally friendly adhesive systems can do

READ NOW

PRESENTED BY
 **MASTERBOND**
ADHESIVES | SEALANTS | COATINGS



Vortex shedding suppression in mixed convective flow past a square cylinder subjected to large-scale heating using a non-Boussinesq model

Cite as: Phys. Fluids 31, 023602 (2019); doi: 10.1063/1.5079516

Submitted: 31 October 2018 • Accepted: 9 January 2019 •

Published Online: 4 February 2019



Md. Reyaz Arif^{a)}  and Nadeem Hasan^{b)} 

AFFILIATIONS

Computational Fluid Dynamics Laboratory, Mechanical Engineering Department, Zakir Husain College of Engineering and Technology, Aligarh Muslim University, Aligarh 202002, Uttar Pradesh, India

^{a)}Electronic mail: reyazarif@zhcet.ac.in

^{b)}Electronic mail: nadhasan@gmail.com

ABSTRACT

In the present work, numerical simulations are performed to investigate the vortex shedding suppression phenomenon for mixed convective flows past a square cylinder in the large-scale heating regime. A full compressible flow model with variable transport and thermo-physical properties is employed to capture large-scale heating effects. The Reynolds number, Prandtl number, and Mach number are kept constant at $Re = 100$, $Pr = 0.71$, and $M = 0.1$, while the cylinder inclination (ϕ), free-stream inclination (α), and over-heat ratio (ϵ) are varied in the range $[0, 45^\circ]$, $[0, 90^\circ]$, and $[0, 2]$, respectively. The governing equations are solved numerically using the particle velocity upwind (PVU-M+) scheme. The buoyancy parameter which governs the vortex shedding suppression process in the non-Boussinesq model is identified as $Ri^{NB} = \frac{\epsilon}{Fr^2} \left(\frac{2}{2+\epsilon} \right)$, where Fr is the Froude number. Using the Stuart-Landau model, the neutral curves separating the steady and unsteady flow regimes are generated in the ϵ - ϕ and ϵ - α parametric spaces. The neutral curves show qualitatively similar characteristics as observed for Boussinesq models. The relative contribution of various large-scale heating effects in suppression of vortex shedding is also highlighted. This reveals that buoyancy effects followed by variations in transport properties play a major role in suppression of vortex shedding. The findings are also applicable to a range of low Re ($O(100)$) as supported by data obtained at $Re = 130$ for $\phi = 40^\circ$. The mechanism of vortex shedding suppression has been analyzed and extended for the large-scale heating scenarios.

Published under license by AIP Publishing. <https://doi.org/10.1063/1.5079516>

I. INTRODUCTION

The study of fluid flow past bluff bodies is a topic of interest for researchers, engineers, and scientists due to its wide range of applications in the design of thermal and structural systems. Its applications in design of thermal systems include heat exchangers, extended surfaces, cooling of electronic devices, chemical reactors, cooling towers, and combustion chambers.¹⁻⁴ Applications in structural designs include design of bridges, tall buildings, stadiums, oil pipeline, and chimney stacks.⁵⁻⁷ The two most extensively studied canonical

bluff body geometries are those of circular and square cylinders.⁸⁻¹¹ These geometries represent both smooth and non-smooth shapes with sharp corners. The flow past a square cylinder differs from that of the circular counterpart as the separation points are fixed on the corners of the cylinder.¹¹⁻¹³ It is well known that the structure and dynamics of the flow past a cylinder depends on the Reynolds number ($Re = U_\infty d/\nu$), where U_∞ is the free-stream velocity, d is the characteristic size of the cylinder, and ν is the kinematic viscosity of fluid. As Re is increased from very low values ($O(1)$), at a critical Reynolds number which depends on the geometry of

bluff bodies, there is onset of vortex shedding. For an unheated square as well as a circular cylinder, the critical Reynolds number for the onset of vortex shedding is well established and lies in a narrow range $Re = 40\text{--}47$.^{14,15} Vortex shedding results in alternate periodic shedding of vortices of opposite sense generating the well-known Karman vortex street. Vortex shedding is desirable from the point of heat transfer, mixing enhancement, structural vibrations, and stability. The suppression of vortex shedding is sometimes preferable, as to reduce the vortex-induced vibration caused by fluctuating forces on the cylinder that may lead to failure of the structure, particularly if the vortex shedding frequency matches with that of structural frequency. Thus, there is a need for the control of vortex shedding phenomena.

The methods employed for the control of vortex shedding are broadly divided into (i) passive and (ii) active control methods. The passive control methods are those which do not need any external energy for its applications. They include suppression of vortex shedding by modifying the body structure, such as providing roughness to the surface of the cylinder, placement of a small control cylinder in the wake region, by using porous and permeable walls, and by introducing splitter plates. The active control methods are the energy consuming methods. They involve the control of vortex shedding by using thermal effects, plasma actuators, by rotation, and oscillation of the cylinder. The details of the various control methods are given in the review paper of Choi *et al.*¹⁶ and the recent reviews by Rashidi *et al.*¹⁷

The active control technique involving thermal effects has been employed for vortex-shedding suppression.^{18–22} In comparison to the isothermal scenario, the scenario of fluid flow past a bluff body coupled with heat exchange involves more complicated physics owing to the possibilities of various thermal effects like (i) significant variations in fluid density across different fluid particles (stratification) under the influence of gravity giving rise to buoyancy forces, (ii) significant volumetric straining effects in individual fluid particles and their consequences on momentum and energy transport, and (iii) variations in molecular transport and thermo-physical properties caused by large temperature variations.

Most of the studies on non-isothermal flows have focused only on the effects of stratification and buoyancy forces. Such effects are typically modelled via the Oberbeck-Boussinesq (OB) approximation where both volumetric straining effects and variations in transport/thermo-physical properties of the fluid are neglected. These simplifying approximations limit the use of OB models to scenarios involving small scale temperature variations. However there are flows where large-scale heating is involved such as in the field of electronic packaging, chimneys, and heat treatment processes of metals like annealing. In order to model such scenarios, the non-Boussinesq fluid flow model must be used.²³ In such a model, volumetric straining effects ($\nabla \cdot \vec{V} \neq 0$) with variable transport and thermo-physical properties must be considered. No studies are available in the literature for mixed convective flows past cylinders using Non-Oberbeck-Boussinesq (NOB) models.

The problem of mixed convective flow past a square cylinder has several aspects. Vortex shedding characteristics, aerodynamic, and heat transfer characteristics are the three main aspects that warrant attention. Figure 1 shows the schematic diagram of two-dimensional (2D) flow around a square cylinder in the mixed convection regime. The free-stream velocity and temperature are denoted by U_∞ and T_∞ , respectively. The cylinder temperature is denoted by T_w which is higher than T_∞ . The free-stream inclination and the cylinder inclination are denoted by α and ϕ , respectively. In the presence of gravitational effects, these two angles behave as independent parameters and hence both need to be considered separately. The mixed convective flow around a heated/cooled square cylinder involves a number of dimensionless control parameters, namely, the flow Reynolds number (Re), the Prandtl number (Pr), the cylinder inclination (ϕ), and the free-stream inclination (α) (Fig. 1). For small scale heating scenarios ($\frac{T_w - T_\infty}{T_\infty} \ll 1$), the Boussinesq model results in a single buoyancy force dimensionless parameter known as Richardson number (Ri). However, as highlighted in the work of Hasan and Saeed,²⁴ the large-scale heating scenario is governed by the full compressible flow equations with specific heat ratio, γ , and flow Mach number, M , as an additional parameter in addition to Re and Pr . The heating and buoyancy effects are characterized by additional dimensionless parameters, namely, the over-heat ratio, $\epsilon = (T_w - T_\infty)/T_\infty$, and Froude number, $Fr = U_\infty/\sqrt{gd}$. It is evident that the large-scale heating scenario involves an extended non-dimensional parametric space and therefore is a challenging problem.

Studies carried out earlier for flows subjected to small and large scale heating around a cylinder of the square cross section are reviewed in brief in order to spell out the gaps and to justify the objectives (as mentioned later) of the present study. In a series of numerical investigations, Sharma and Eswaran^{25,26} investigated vortex shedding and heat transfer

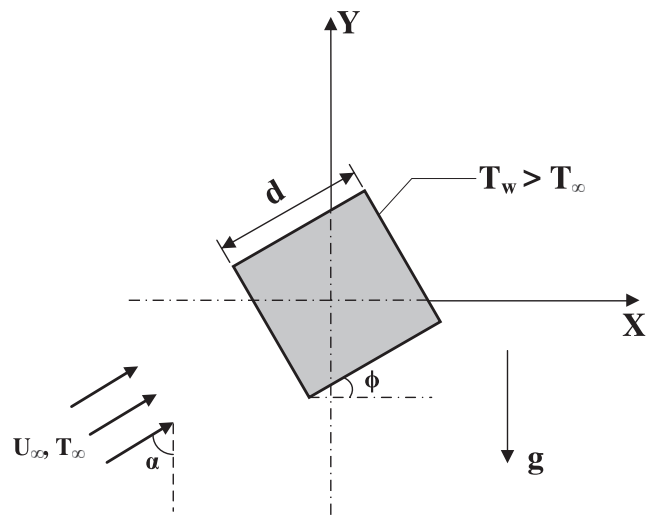


FIG. 1. Schematic diagram of flow problem.

characteristics for the flows past a cylinder of the square cross section in the mixed convection regime employing the Boussinesq approximation for $\alpha = \phi = 0^\circ$ at $Re = 100$ and $Pr = 0.71$. For the case of aiding buoyancy, they showed that the vortex shedding suppression takes place at $Ri = 0.15$. Furthermore, they investigated the buoyancy effects on flow past a square cylinder for both cooling and heating scenarios by varying Ri in the range $[-1, 1]$. In another numerical investigation, Sharma and Eswaran²⁷ investigated the mixed convective flow of air past a square cylinder in cross flow ($\alpha = 90^\circ, \phi = 0^\circ$) for both steady and unsteady periodic laminar flow regimes by varying Re in the range $[1, 160]$. They studied the effect of vortex shedding on the isotherm patterns and developed the heat transfer correlations between the Nusselt number and Reynolds number for two different boundary conditions (i) uniform heat flux and (ii) constant cylinder temperature.

Bhattacharyya and Mahapatra²⁸ performed two-dimensional numerical simulations employing the Boussinesq approximation and studied the effect of buoyancy on the vortex shedding phenomena past a heated square cylinder in a cross flow configuration ($\alpha = 90^\circ, \phi = 0^\circ$). The flow parameters were chosen as $Pr = 0.72, 0 \leq Ri \leq 1$, and Re was varied up to 1400. They found that the vortex shedding around a square cylinder occurs at Re greater than 40. They also found that the vortex shedding is not suppressed for any value of buoyancy in the cross flow.

Turki *et al.*²⁹ investigated numerically the vortex shedding and heat transfer characteristics in an unsteady two-dimensional flow in a horizontal channel ($\alpha = 90^\circ$) with a built-in heated square cylinder ($\phi = 0^\circ$) employing the Boussinesq approximation. They considered two values of Blockage ratio (Br) $1/4$ and $1/8$. The Reynolds and Richardson numbers were varied in ranges given as $62 \leq Re \leq 200, 0 \leq Ri \leq 0.1$. From their study, they found that for a mixed convective flow, the Strouhal number (i.e., vortex shedding frequency) increases with an increase in Re and the Nusselt number increases with an increase in Ri .

Employing a Boussinesq model, Chatterjee and Mondal³⁰ performed numerical simulations to study the effect of thermal buoyancy on the vortex shedding characteristics in two-dimensional cross flow ($\alpha = 90^\circ$) past an unconfined cylinder of the square cross section at low Re . The ranges of various dimensionless parameters were chosen as $5 \leq Re \leq 40, 0 \leq Ri \leq 2, Pr = 0.7$, and $Br = 0.05$. They found that an increase in Ri triggered vortex-shedding and the critical Ri decreases with increasing Re for the onset of vortex shedding.

Dulhani *et al.*,³¹ using a Boussinesq model, numerically studied the aerodynamic characteristics of mixed convective cross flow ($\alpha = 90^\circ$) of air past a square cylinder in the range $-1 \leq Ri \leq 1$ at $Re = 100$. The cylinder orientation was also varied in the range $0 \leq \phi \leq 45^\circ$. They concluded that with increasing ϕ , the lateral width of the cylinder wake reduces. For all angles of incidence (ϕ), the coefficient of drag (C_D) reduces with increasing Ri , while the coefficient of moment (C_M) increases linearly with increasing Ri .

In a recent study, Hasan and Ali³² investigated the role of baroclinic vorticity in the wake of the heated bluff bodies in suppression of vortex shedding. Employing a Boussinesq model, the steady and the unsteady flow regimes were separated out by identifying the neutral curves for the circular as well as the square cylinder in the parametric space of Ri - α . Furthermore, a phenomenological model was proposed for suppression of vortex shedding by thermal buoyancy. The model successfully predicted the mathematical characteristics of the numerically obtained neutral curves. Their phenomenological model for vortex shedding suppression by thermal buoyancy represents the first attempt at uncovering the underlying mechanism of vortex shedding suppression for the flows past heated bluff obstacles in the mixed convection regime.

Rahnama and Hadi-Moghaddam³³ performed 2D numerical simulations and studied the heat and fluid flow of air over a square cylinder placed in a channel having blockage ratio $1/8$ and $Re \leq 200$ in the forced convection regime. Their findings show that the recirculation length increases and the drag coefficient decreases as Re increases until $Re = 100$. Beyond $Re = 100$, the drag coefficient increases until $Re = 200$. They also showed that at low Re ($Re < 200$), unsteadiness in the Nusselt number due to vortex shedding is negligible.

A numerical investigation of 2D forced convective flow and heat transfer past an inclined square cylinder ($0 \leq \phi \leq 45^\circ$) in a low Reynolds number regime ($Re = 60, 100$, and 150) for $Pr = 0.71$ was carried out by Ram *et al.*³⁴ The unsteady, incompressible flow model with constant transport and thermophysical properties was used. They found that there was an increase in Strouhal number as one increases Re and ϕ . They also showed that the mean Nu increases with an increase in Re and ϕ .

Ambreen and Kim³⁵ performed two-dimensional numerical simulations, and studied the various aerodynamic and heat transfer characteristics for laminar forced convective flow ($\alpha = 90^\circ, \phi = 0^\circ$) of air over a heated cylinder of the square cross section having four different types of corner geometries, namely, sharp, round, chamfered, and recessed for $55 \leq Re \leq 200$. Using the Boussinesq model, they showed that there is reduction in the average coefficient of drag but the Strouhal number and the mean Nusselt number increase by modifying the corners.

Kakade *et al.*³⁶ experimentally studied the combined effects of cylinder inclination and buoyancy (small-scale heating) for a cylinder of the square cross section on vortex shedding and wake characteristics. The experiments were performed for $Re = 56, 87$, and 100 , while the Richardson number and cylinder inclination were varied in the range of $[0.031, 0.291]$ and $[0, 45^\circ]$, respectively. They showed that for a given Reynolds number, as the incidence angle increases up to $\phi = 20^\circ$, the critical Richardson number increases and beyond $\phi = 20^\circ$ it remains nearly constant.

All the studies mentioned above are restricted to small-scale heating, and the numerical studies utilize the Boussinesq approximation. Some of the researchers have studied the large-scale heating scenarios in the forced convection regime for circular cylinders. Sabanca and Durst³⁷

used a non-Boussinesq model by considering the variation of viscosity coefficient, μ , and thermal conductivity, κ , with temperature to study the forced convective flow past a circular cylinder having slight compressible effects. Shi *et al.*³⁸ performed numerical experiments to study the forced convective flow past a heated circular cylinder with high heating effects using an incompressible solver by including the transient density term in the continuity equation and using variable transport and thermo-physical variables. They however neglected the volumetric straining effects in their model.

The first attempt to systematically study the effects of large-scale heating on forced convective 2D flow past a square cylinder using a full NOB flow model (accounting for volumetric straining effects) was made by Hasan and Saeed.²⁴ They studied the combined effects of heating and free-stream inclination and showed that it is necessary to use a compressible flow model in order to predict accurately the Nusselt number and aerodynamic forces for $\epsilon \geq 0.1$ and $\epsilon \geq 0.2$, respectively. To the best of the authors' knowledge, no other numerical studies are available in the literature pertaining to the flow past a heated square cylinder using a non-Boussinesq model. In particular, the mixed convective flow past a heated square or circular cylinder in the large-scale heating regime has not been investigated earlier.

The present work is the first attempt to numerically explore the vortex shedding characteristics in mixed convective flow past a square cylinder at a low Reynolds number using a non-Boussinesq model, in order to account for all the large-scale heating effects. A non-Boussinesq model (compressible flow model with variable transport and thermophysical properties) is employed to capture large-scale heating effects in the low-speed flow. Air is treated as a thermally perfect gas obeying the ideal gas equation of state. All the computations are performed at a fixed Reynolds number of $Re = 100$ and a low free-stream Mach number, $M = 0.1$, so as to minimize any pressure compressibility effects. The cylinder inclination, ϕ , is varied in the range $[0, 45^\circ]$, and the free-stream inclination, α , is varied in the range $[0, 90^\circ]$. The over-heat ratio, ϵ , is varied in the interval $[0, 2]$. The objectives of the present work are as follows:

- Identification of an equivalent Richardson number type parameter which governs the vortex shedding suppression process in large-scale heating scenarios.
- Investigation of the effect of cylinder inclination, ϕ , and free-stream inclination, α , on vortex shedding suppression and to identify the neutral curves separating the steady and unsteady flow regimes in the parametric space of ϵ - ϕ and ϵ - α .
- To identify the relative importance of physical effects like variations in density, variations in transport properties, specific heat in influencing the vortex shedding suppression characteristics, or the neutral curves in ϵ - ϕ and ϵ - α parametric spaces.
- Identification of similarities and differences in the vortex shedding mechanism in the large scale heating regime vis-a-vis a small scale heating scenario

(governed by Boussinesq models) already reported in Ref. 32.

II. MATHEMATICAL MODELING

The unconfined flow past a heated square cylinder is modeled by considering a two-dimensional, unsteady, viscous, and laminar compressible flow of air. In low speed flows, heating effects are generally studied using two distinct classes of models. The first class deals with small-scale heating models, commonly known as Oberbeck-Boussinesq models (OB models), while the second class is that of the large-scale heating models, may be called Non-Oberbeck-Boussinesq models (NOB models). The OB model can be used only when $(\beta\Delta T) \ll 1$, where β is the thermal expansion coefficient and ΔT is the imposed temperature difference scale. In the OB model, the density changes in the fluid can be neglected except in the gravity terms, where ρ is multiplied with gravity (g). This model neglects the effects of thermal straining in the individual fluid particles. In addition, the variations in molecular transport and thermo-physical properties such as viscosity, thermal conductivity, and specific heats with temperature are neglected. On the other hand, the NOB model may be used for buoyancy-driven flows with large temperature gradients, especially while dealing with gases. In this model $(\beta\Delta T) \sim O(1)$, the various large-scale heating effects like volumetric thermal straining, variations in molecular transport, and thermo-physical properties are accounted for in this model. In the present work, an NOB model has been employed to capture the large-scale heating flow physics.

A. Governing equations

The equations of compressible gas flows are used as the governing equations. The dimensionless governing equations, written in strong conservative forms in 2D Cartesian coordinates, are given as²⁴

$$\frac{\partial \mathbf{U}}{\partial t} + \frac{\partial \mathbf{F}}{\partial x} + \frac{\partial \mathbf{G}}{\partial y} = \mathbf{J}, \quad (1)$$

where the vectors \mathbf{U} , \mathbf{F} , \mathbf{G} , and \mathbf{J} appearing in Eq. (1) are the solution, the flux, and the source vectors, respectively.

These vectors are:

$$\mathbf{U} = \begin{Bmatrix} \rho \\ \rho u \\ \rho v \\ \rho E \end{Bmatrix}, \quad (2)$$

$$\mathbf{F} = \begin{Bmatrix} \rho u \\ \rho u^2 + p - \frac{2\mu}{Re} \left\{ \frac{\partial u}{\partial x} - (\nabla \cdot \vec{V})/3 \right\} \\ \rho uw - \frac{\mu}{Re} \left(\frac{\partial v}{\partial x} + \frac{\partial u}{\partial y} \right) \\ \rho uE - \frac{\gamma}{RePr} \left(k \frac{\partial T}{\partial x} \right) + \phi^F \end{Bmatrix}, \quad (3)$$

$$\mathbf{G} = \begin{pmatrix} \rho v \\ \rho uv - \frac{\mu}{Re} \left(\frac{\partial v}{\partial x} + \frac{\partial u}{\partial y} \right) \\ \rho v^2 + p - \frac{2\mu}{Re} \left\{ \frac{\partial v}{\partial y} - (\nabla \cdot \vec{V})/3 \right\} \\ \rho v E - \frac{\gamma}{RePr} \left(k \frac{\partial T}{\partial y} \right) + \phi^G \end{pmatrix}, \quad (4)$$

$$\mathbf{J} = \begin{pmatrix} 0 \\ 0 \\ (1-\rho)/Fr^2 \\ \gamma(\gamma-1) \left(\frac{M}{Fr} \right)^2 (1-\rho)v - (\gamma-1)(\nabla \cdot \vec{V}) \end{pmatrix}, \quad (5)$$

where the terms ϕ^F and ϕ^G are given by $\phi^F = \gamma(\gamma-1)M^2[p u + (\mu/Re)D_F]$ and $\phi^G = \gamma(\gamma-1)M^2[(p v + (\mu/Re)D_G)]$, respectively. The symbols u , v , ρ , p , and E represent the non-dimensional x and y velocity components of fluid, density, pressure, and total energy, respectively. Note that these equations are expressed in a manner that contain the buoyancy terms explicitly in momentum and energy equations. The quantities D_F and D_G are given as

$$D_F = \left[\frac{2}{3} u \left(\frac{\partial v}{\partial y} - 2 \frac{\partial u}{\partial x} \right) - v \left(\frac{\partial v}{\partial x} + \frac{\partial u}{\partial y} \right) \right], \quad (6)$$

$$D_G = \left[\frac{2}{3} v \left(\frac{\partial u}{\partial x} - 2 \frac{\partial v}{\partial y} \right) - u \left(\frac{\partial v}{\partial x} + \frac{\partial u}{\partial y} \right) \right]. \quad (7)$$

For closure of the above governing equations, the various state relations are used. Its non-dimensional form, assuming air as a thermally perfect gas ($\gamma = 1.4$) is as follows:

$$\rho = \frac{1 + \gamma M^2 p}{T}, \quad e = \int_1^T C_v(T) dT + e_o, \quad E = e + \frac{\gamma(\gamma-1)}{2} M^2 (u^2 + v^2). \quad (8)$$

In these equations e , T , and C_v are the dimensionless specific internal energy, temperature, and constant volume specific heat, respectively. The various dimensionless flow variables are defined as $u = \bar{u}/U_o$, $v = \bar{v}/U_o$, $\rho = \bar{\rho}/\rho_o$, $T = \bar{T}/T_o$, $p = (\bar{p} - \bar{p}_o)/\rho_o U_o^2$, $e = \bar{e}/C_{v0} T_o$, $e_o = \bar{e}_o/C_{v0} T_o$, $E = \bar{E}/C_{v0} T_o$, $\mu = \bar{\mu}/\mu_o$, $k = \bar{k}/k_o$, $C_v = \bar{C}_v/C_{v0}$, $t = \bar{t} U_o/d$, $x = \bar{x}/d$, and $y = \bar{y}/d$.

The reference state values are represented by the subscript "o." In the whole text, the subscript " ∞ " represents the isothermal free-stream condition which is taken as a reference. The dimensional variables are indicated by over bars. The term e_o appearing in the specific internal energy relation of the state equation denotes the datum level and is taken as unity, i.e., $\bar{e}_o = \bar{e}_\infty = C_{v0} T_\infty$.

In the present model, the molecular transport property such as $\bar{\mu}$, \bar{k} , and the specific heats, \bar{C}_v , are chosen as functions of temperature only. This is due to the fact that at a low Mach number, pressure variations are small and for the ideal gases the specific heats are functions of temperature only.

The viscosity variation with temperature is prescribed through the Sutherland viscosity relation, which is given by

$$\frac{\bar{\mu}}{\bar{\mu}_o} = \left(\frac{\bar{T}}{\bar{T}_{sr}} \right)^{3/2} \left(\frac{\bar{T}_{sr} + S}{\bar{T} + S} \right). \quad (9)$$

The dimensionless form of Eq. (9) can be written as

$$\mu = T^{3/2} \left(\frac{T_r + \sigma}{T T_r + \sigma} \right), \quad (10)$$

where $T_r = \bar{T}_\infty/\bar{T}_{sr}$, $\sigma = S/\bar{T}_{sr}$, and \bar{T}_∞ is the free-stream temperature. S is Sutherland's constant, and its value is 110 K, while \bar{T}_{sr} is Sutherland's reference temperature which is equal to 273 K. The dimensionless specific heat at constant volume and thermal conductivity is taken to be functions of temperature given as

$$C_v = 1 + A_1(T-1) + A_2(T-1)^2 + A_3(T-1)^3, \quad (11)$$

$$k = a + bT + cT^2. \quad (12)$$

The dimensionless specific internal energy is given as

$$e = T + A_1(T-1)^2/2 + A_2(T-1)^3/3 + A_3(T-1)^4/4. \quad (13)$$

The various constants in Eqs. (11)–(13) are $A_1 = 1.201 \times 10^{-2}$, $A_2 = 6.528 \times 10^{-2}$, $A_3 = -1.576 \times 10^{-2}$ and $a = 2.811 \times 10^{-2}$, $b = 1.074$, $c = -9.918 \times 10^{-2}$. These constants have been taken from Ref. 24, which are based on property data reported in Ghoshdastidar.³⁹ These constants are applicable for a wide range of temperatures, i.e., [300 K, 1000 K] with $\bar{T}_\infty = 300$ K as a reference. The relation of temperature as a function of specific heat is obtained using the inverse relation which is derived by fitting the curve of the data (e , T) using Eq. (13) in the range of dimensionless temperatures $1 \leq T \leq 3$ and is given as

$$T = -0.049 + 1.082e - 0.034e^2 - 2.882 \times 10^{-4}e^3. \quad (14)$$

The transformed governing equations in body-fitted curvilinear coordinates (ξ , η) along with physical boundary and initial conditions are given in Appendix A.

B. Numerical boundary conditions

By applying numerical boundary conditions, the solution vector $\mathbf{U} = [\rho, \rho u, \rho v, \rho E]^T$ is updated at any point on the far boundary. The characteristic numerical boundary conditions based on wave speeds of Euler equations along the local normal direction are employed. These boundary conditions are discussed in detail by Hirsch⁴⁰ and were also employed in Ref. 24. The boundary conditions are summarized in Tables I and II.

The unit vectors representing the free stream flow direction and the inward geometric normal to the far boundary are indicated as \hat{i}_∞ and \hat{n}_G in Table I. Thus an inflow portion is characterized by $\hat{i}_\infty \cdot \hat{n}_G > 0$ and an outflow portion by $\hat{i}_\infty \cdot \hat{n}_G < 0$. The local unit normal for flow, \hat{n}_F , is taken inwards at the inflow portion ($\hat{n}_F = \hat{n}_G$) and outwards at the outflow portion ($\hat{n}_F = -\hat{n}_G$) so that the local normal velocity

TABLE I. Inflow and outflow boundary conditions.

Inflow ($\hat{i}_\infty \cdot \hat{n}_G > 0$)	Outflow ($\hat{i}_\infty \cdot \hat{n}_G < 0$)
1. Acoustic waves $V_N + c > 0; (R_N^+)_B = (R_N^+)_\infty$ $V_N - c < 0; (R_N^-)_B = (R_N^-)_i$	1. Acoustic waves $V_N + c > 0; (R_N^+)_B = (R_N^+)_i$ $V_N - c < 0; (R_N^-)_B = (R_N^-)_\infty$
2. Shear wave $V_N > 0, (V_T)_B = (V_T)_\infty$	2. Shear wave $V_N > 0, (V_T)_B = (V_T)_i$
3. Entropy wave $V_N > 0, \rho_B = (T_B)^{1/(\gamma-1)}$	3. Entropy wave $V_N > 0, \frac{\partial \rho}{\partial t} + (V_N + c) \frac{\partial \rho}{\partial \eta} = 0$

component $V_N = (\vec{V} \cdot \hat{n}_f)$ is positive for both inflow and outflow. The local normal acoustic wave speeds are $V_N \pm c$, where V_N and c are the local dimensionless normal component of flow velocity and the local dimensionless speed of sound. The local normal wave speeds of the four family of waves (two acoustic, one shear, and one entropy) are utilized to fix the four related variables; the two Riemann invariants $R_N^\pm = V_N \pm \frac{2\sqrt{T}}{M(\gamma-1)}$, local tangential velocity V_T , and density " ρ " at any point on the inflow/outflow portion of the boundary, as indicated in Table I. The subscript "B" indicates the value at a boundary point, while "i" indicates the interpolated value from the interior data. Once the Riemann invariants are obtained at the boundary; the values of the normal velocity and temperature are obtained as

$$(V_N)_B = \frac{(R_N^+)_B + (R_N^-)_B}{2}; \quad T_B = \frac{M^2 [(R_N^+)_B - (R_N^-)_B]^2}{4(\gamma-1)^2}. \quad (15)$$

The interpolated values of R_N^\pm are obtained using two interior points and by setting the second derivative of R_N^\pm equal to zero along the η -direction. The interpolated value of tangential velocity $(V_T)_i$ at outflow is obtained by first obtaining an interpolated value of the vorticity component Ω_z at the boundary. Then, since $(\Omega_z)_B = \left(\frac{\partial V_N}{\partial T}\right)_B - \left(\frac{\partial V_T}{\partial n}\right)_B$, the value of the normal derivative of the tangential component of velocity (V_T) can be computed from the derivative $\left(\frac{\partial V_N}{\partial T}\right)_B$ as the normal component of velocity has been updated at all points on the boundary. Finally, the one sided second order discretization of $\left(\frac{\partial V_T}{\partial n}\right)_B$ is utilized to obtain the boundary value of the tangential component of velocity $(V_T)_B$. The values of V_N and V_T are eventually converted into the Cartesian components (u, v).

TABLE II. Pressure boundary conditions for inflow and outflow.

Inflow ($\hat{i}_\infty \cdot \hat{n}_G > 0$)	Outflow ($\hat{i}_\infty \cdot \hat{n}_G < 0$)
1. $V_N = 0$	$V_N = 0$
2. $V_T = V_{T_\infty}$	V_T extrapolated by setting $\frac{\partial V_T}{\partial n} = 0$
3. $p = 0$ (free-stream condition)	$p =$ extrapolated from interior

These characteristic boundary conditions work well so long as the magnitude of the local normal component of velocity is above a certain small threshold value. This is because for very small V_N , the characteristic speeds of entropy/shear waves become negligibly small in comparison to the acoustic wave speeds. This results in a numerical stiffness locally in the usual characteristic boundary conditions. This stiffness shows up in the form of accumulation of numerical errors and spurious reflection from locations when V_N is very small. Therefore, a different set of BC's as indicated in Table II are employed at points, where $|V_N| < \delta$. Using the value of pressure from Table II, density and temperature are evaluated from $\rho = (1 + \gamma M^2 p)/T$ and $T = (1 + \gamma M^2 p)^{(\gamma-1)/\gamma}$, respectively. The expression for temperature is a statement of entropy preservation between the free-stream and the boundary point under consideration. A threshold value of $\delta = 5 \times 10^{-2}$ is found to be suitable to eliminate the spurious boundary reflections.

C. Dimensionless parameters

In the non-Boussinesq formulation, there are a number of dimensionless control parameters that occur either in the governing equations, the boundary conditions and the geometric configuration of the problem. These control parameters are mentioned by

- (i) Reynolds number, $Re \equiv \rho_\infty U_\infty d / \mu_\infty$,
- (ii) Mach number, $M \equiv U_\infty / a_\infty$,
- (iii) Froude number, $Fr \equiv U_\infty / \sqrt{gd}$,
- (iv) Prandtl number, $Pr \equiv \mu_\infty \gamma C_{v\infty} / k_\infty$,
- (v) Specific heat ratio, $\gamma \equiv C_{p\infty} / C_{v\infty}$,
- (vi) Over-heat ratio, $\epsilon \equiv (T_w - T_\infty) / T_\infty$,
- (vii) Sutherland parameters (a) $T_r \equiv \bar{T}_\infty / \bar{T}_{sr}$ and (b) $\sigma \equiv S / \bar{T}_{sr}$,
- (viii) Free-stream inclination $\equiv \alpha$, and
- (ix) Cylinder inclination $\equiv \phi$.

In the mixed convection flow, since the gravitational effect would also be taken into account, therefore the orientation of fluid flow (α) with respect to gravity vector and the inclination of the cylinder (ϕ) will act as independent parameters. Unless mentioned otherwise, all the computations reported in the present work have been carried for $\alpha = 0^\circ$, $Re = 100$, $M = 0.1$, $T_\infty = 300$ K, $\gamma = 1.4$, and $Pr = 0.71$.

There are dimensionless output parameters such as aerodynamic parameters (coefficients of lift and drag), heat transfer parameter (Nusselt number), and frequency of vortex shedding (Strouhal number) that are recorded. The definitions of these output parameters are given in Appendix B.

III. NUMERICAL METHODOLOGY AND VALIDATION

In the present section, the grid generation methods, the numerical scheme, and the numerical aspects such as the sensitivity to the location of far boundary, grid, and the time step are discussed in detail. This is followed by validation studies carried out in order to assess the accuracy of the numerical computations.

A. Grid generation

A body-fitted structured grid of O-type is used in the numerical simulations. The advantage of using this type of grid is that it adapts to the geometry of the bodies, i.e., body of any shape can be fitted to this type of grid. The O-type grid completely surrounds the body under consideration. The methods used for generating this type of grid are well established and

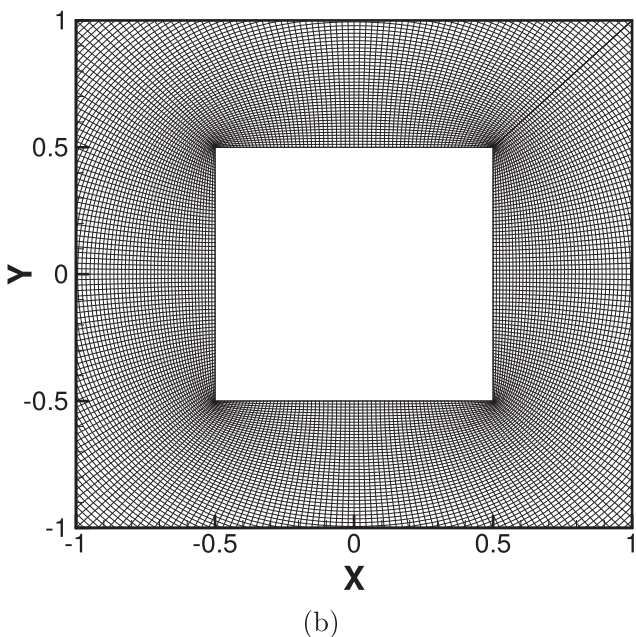
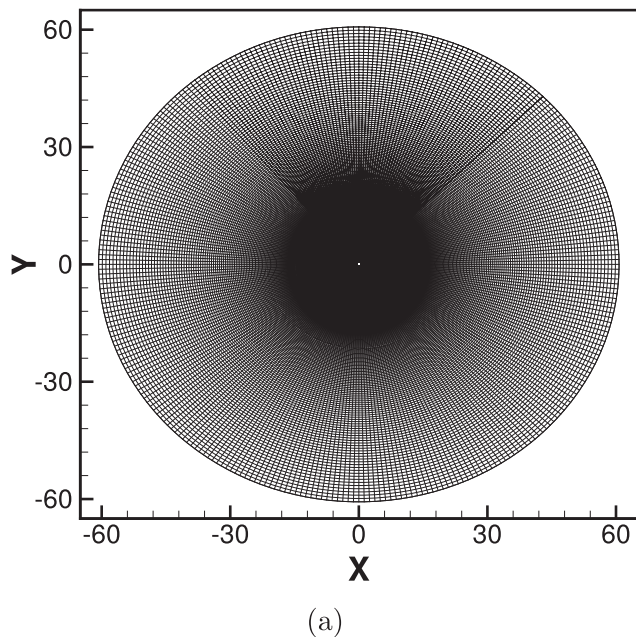


FIG. 2. Computational grid around the square cylinder. (a) O-type grid and (b) enlarged view of the grid near the cylinder.

are given in Thompson *et al.*⁴¹ The grid obtained by the above process is shown in Fig. 2. The grid used in the entire computations contains 305 points in the ξ direction and 375 points in the η directions, having a dimensionless near cylinder spacing of 1.8×10^{-3} .

In order to transform the doubly connected physical plane to the rectangular singly connected computational plane, a cut is made starting on the inner boundary and extending to the outer boundary. The suitable location of the cut is important to minimize any discretization error which may arise due to any asymmetry of grid with respect to the free-stream orientation. Figure 3 shows the cut which is made at any arbitrary angle, θ . The cut when located at $\theta = 45^\circ$ with respect to the X-axis is found to be most suitable for the numerical simulations. This is inferred by performing two numerical experiments with forced convection, one at free-stream orientation $\alpha = 0^\circ$ and the other with free-stream orientation $\alpha = 90^\circ$. As shown in Fig. 4 that the variation of C_L and C_D with time for forced convection at $\alpha = 0^\circ$ and $\alpha = 90^\circ$, respectively, matches with each other. Hence the grid having cut at $\theta = 45^\circ$ is suitable for carrying out computations for $0 \leq \alpha \leq 90^\circ$. This is an important numerical aspect as changes in free-stream inclination should not induce significant discretization errors due to overall grid asymmetry with respect to the incoming free-stream direction.

B. Numerical scheme

In the present work, all the computations are performed using the latest version particle velocity upwind scheme (PVU-M+) which is a flux based scheme for compressible flows,

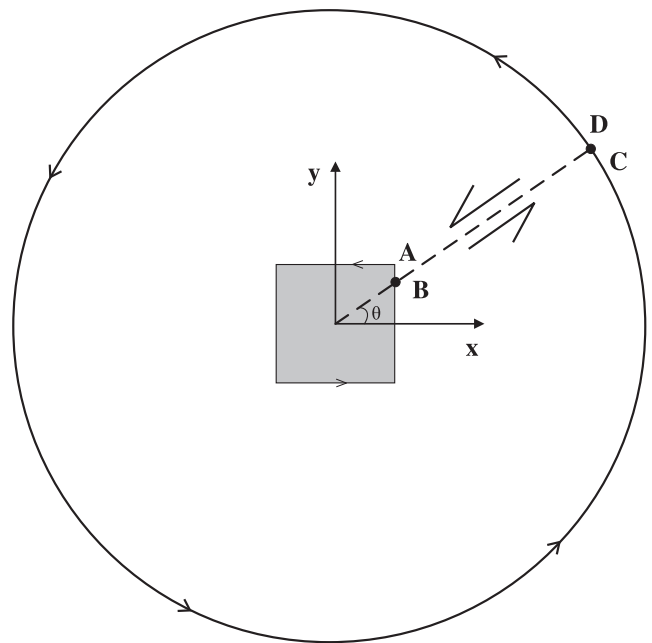


FIG. 3. A sketch showing cut made in the grid.

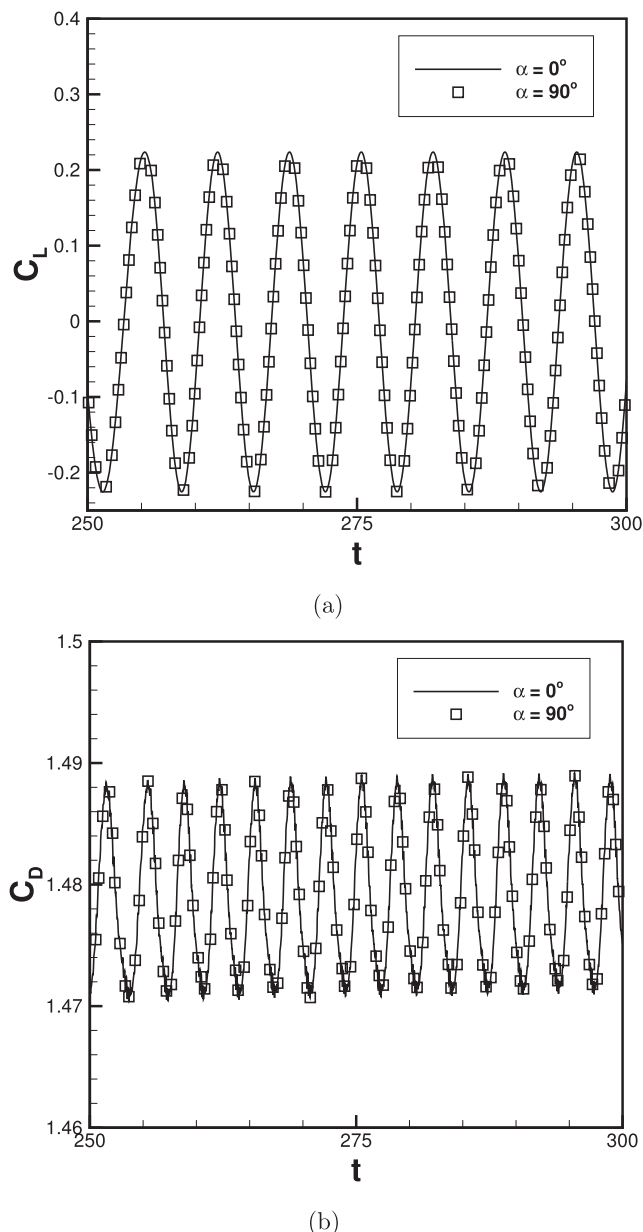


FIG. 4. (a) C_L vs time and (b) C_D vs time for forced convection at $\alpha = 0^\circ$ and $\alpha = 90^\circ$ using the grid with $\theta = 45^\circ$ cut.

governed by Euler/Navier-Stokes equations.⁴² It is an improved version of the earlier PVU scheme proposed by Qamar *et al.*⁴³ The PVU-M+ scheme is proven to be simple, robust, yet accurate scheme for flows governed by a compressible Euler/Navier-Stokes equation. The main advantage is its simplicity, accuracy, and applicability for a wide range of Mach numbers ($M = 0.1$ – 10), i.e., starting from a nearly incompressible range to a hypersonic range. In the present work, a compressible flow model at a low Mach number ($M \approx 0.1$) is

to be solved numerically. Hence it is justified to use the PVU-M+ scheme. This scheme employs the second order accurate time integration via predictor and corrector steps to determine the solution vector at any grid point (details are given in [Appendix C](#)).

C. Numerical aspects

In this section, the numerical aspects like sensitivity to the location of far boundary, grid size, and the time step are discussed. The various non-dimensional output parameters such as coefficient of drag, Nusselt number, and Strouhal number are used for assessing the sensitivity of these numerical parameters on the overall computations.

The present work is the problem of fluid flow past an unconfined square cylinder. But in order to perform computations, the infinite domain must be truncated by introducing a far boundary. If the far boundary is chosen very near to the cylinder, then the reflection from the artificial boundary due to numerical boundary conditions discussed earlier may cause disturbance to the flow fields and a subsequent loss in accuracy of results. While if the far boundary is at large distance from the cylinder, then it will enhance the computational cost as well as time. Hence there is a need to perform a domain size independence test to get accurate and reliable results. To perform the test, an initial grid of size 241×325 mesh points with far boundary fixed at a non-dimensional distance of 120 from the center of the square cylinder is considered. The numerical simulations are then performed for grids truncated at non-dimensional distances of 20, 40, 60, 80, and 100 from the center of the cylinder, at the same flow conditions ($Re = 100$, $Pr = 0.71$, $Fr = 1.0$, $\epsilon = 0.05$, $\alpha = 0^\circ$, and $\phi = 0^\circ$). The mean coefficient of drag, mean Nusselt number, and the Strouhal number are recorded for all five locations of artificial boundary and are tabulated in [Table III](#). It is observed that from the dimensionless distance of 60 onward, there are negligible changes in the value of C_D , Nu , and St . Hence a suitable location of far boundary is found to be at a dimensionless distance of 60.

The grid independence test is done for both the cases of small-scale heating ($\epsilon = 0.05$) and large-scale heating ($\epsilon = 1.0$) keeping flow parameters as $Re = 100$, $Fr = 1.0$, $Pr = 0.71$, $\alpha = 0^\circ$, and $\phi = 0^\circ$. The far boundary is fixed at a dimensionless distance of 60 from the center of the cylinder. The computations are performed on four different grids, namely, G1, G2, G3, and G4 which consists of 241×325 , 241×375 , 305×375 , and 353×425 grid points, respectively. The results of the grid

TABLE III. Sensitivity to the location of artificial boundary.

Non-dimensional distance	\bar{C}_D	\bar{Nu}	St
20	1.4494	3.9634	0.1201
40	1.4214	3.9433	0.1575
60	1.4124	3.9350	0.1566
80	1.4103	3.9313	0.1569
100	1.4110	3.9303	0.1568

independence test for both cases of small and large scale heating are shown in Tables IV and V, respectively. The results show that the best suited grid for both the cases of low and high heating is G3. Hence the grid G3 is considered for all computations.

The selection of suitable time step for numerical computations is important. In order to select a suitable time step, the numerical simulations are performed at two different time steps, $\Delta t_1 = 1.0 \times 10^{-4}$ and $\Delta t_2 = 5.0 \times 10^{-5}$. The flow parameters are kept the same as $Re = 100$, $Pr = 0.71$, $M = 0.1$, $Fr = 1.0$, $\epsilon = 1.0$, and $\phi = 0 = \alpha$. It is found that the percentage change in the values of average coefficient of drag and average Nusselt number between Δt_1 and Δt_2 simulations is 0.573 and 0.962, respectively, which is very less. Hence the time step of $\Delta t_1 = 1.0 \times 10^{-4}$ is suitable for numerical simulations.

D. Validation

Validation studies are important in order to check the reliability and accuracy of the choice of the numerical method and the various numerical parameters employed. The validation of the present numerical code has already been done and reported for isothermal flow over a square cylinder and forced convective flow around a heated square and circular cylinder in the earlier work of Hasan and Saeed.²⁴ For the mixed convective flow regime, under the non-Boussinesq framework, the present computations are the first of its kind. Hence validation for mixed convective flow can only be carried out with earlier studies employing the Boussinesq model. Therefore, computations are carried out for small ϵ , and the transport property and specific heat variations are not considered in the non-Boussinesq model. The flow parameters used for validation are $Re = 100$, $M = 0.1$, $Pr = 0.71$, $\alpha = 0$, and $\phi = 0$. In validating with data obtained by Boussinesq models, the main issue is to fix the ratio of buoyancy to inertia forces. In Boussinesq models, the ratio of buoyancy to inertia forces is represented directly by the Richardson number given as

$$Ri = \frac{g\beta\Delta Td}{U_\infty^2}, \quad (16)$$

where $\beta = 1/T_\infty$ (perfect gas) is the coefficient of volume expansion and $\Delta T = T_w - T_\infty$.

The expression of Ri can be expressed as

$$Ri = \left(\frac{gd}{U_\infty^2} \right) \cdot \left(\frac{T_w - T_\infty}{T_\infty} \right) = \frac{\epsilon}{Fr^2}. \quad (17)$$

For a non-Boussinesq model, the Richardson type parameter can be expressed as

$$Ri^{NB} = \frac{\text{Buoyancy forces}}{\text{Mean inertia forces}} = \frac{(\rho_\infty - \rho_w)g}{\left(\frac{\rho_\infty + \rho_w}{2} \right) U_\infty^2/d}. \quad (18)$$

For small Mach numbers, $\rho \propto 1/T$; hence,

$$Ri^{NB} \cong \frac{2(T_w/T_\infty - 1)}{(T_w/T_\infty + 1)} \frac{1}{Fr^2}. \quad (19)$$

Thus,

$$Ri^{NB} \cong \frac{\epsilon}{Fr^2} \left(\frac{2}{2 + \epsilon} \right). \quad (20)$$

For $\epsilon \ll 1$, the factor $2/(2 + \epsilon) \sim 1$ so that for small-scale heating,

$$Ri^{NB} \cong \frac{\epsilon}{Fr^2} = Ri. \quad (21)$$

Thus by choosing $Ri^{NB} = Ri$, for small ϵ one establishes a basis of comparing the results obtained by NOB and OB models. The comparison of mean C_D and mean Nu (mean stands for time averaged data) at different $Ri (= Ri^{NB})$ is done with the earlier reported studies,^{25,31,44,45} as shown in Fig. 5. The figures show a good overall agreement.

TABLE IV. Results of the grid independence test for small-scale heating ($\epsilon = 0.05$).

Grid	Grid size	Minimum grid spacing	Maximum grid spacing	$\overline{C_D}$	\overline{Nu}	St
G1	241 × 325	0.002 248	0.013 71	1.4153	3.8784	0.1171
G2	241 × 375	0.001 902	0.011 87	1.4135	3.8839	0.1173
G3	305 × 375	0.001 796	0.011 88	1.4102	3.8995	0.1179
G4	353 × 425	0.001 469	0.010 48	1.4090	3.9075	0.1181

TABLE V. Results of the grid independence test for large-scale heating ($\epsilon = 1.0$).

Grid	Grid size	Minimum grid spacing	Maximum grid spacing	$\overline{C_D}$	\overline{Nu}
G1	241 × 325	0.002 248	0.013 71	2.7296	5.4001
G2	241 × 375	0.001 902	0.011 87	2.6902	5.3875
G3	305 × 375	0.001 796	0.011 88	2.6186	5.2982
G4	353 × 425	0.001 469	0.010 48	2.6112	5.2955

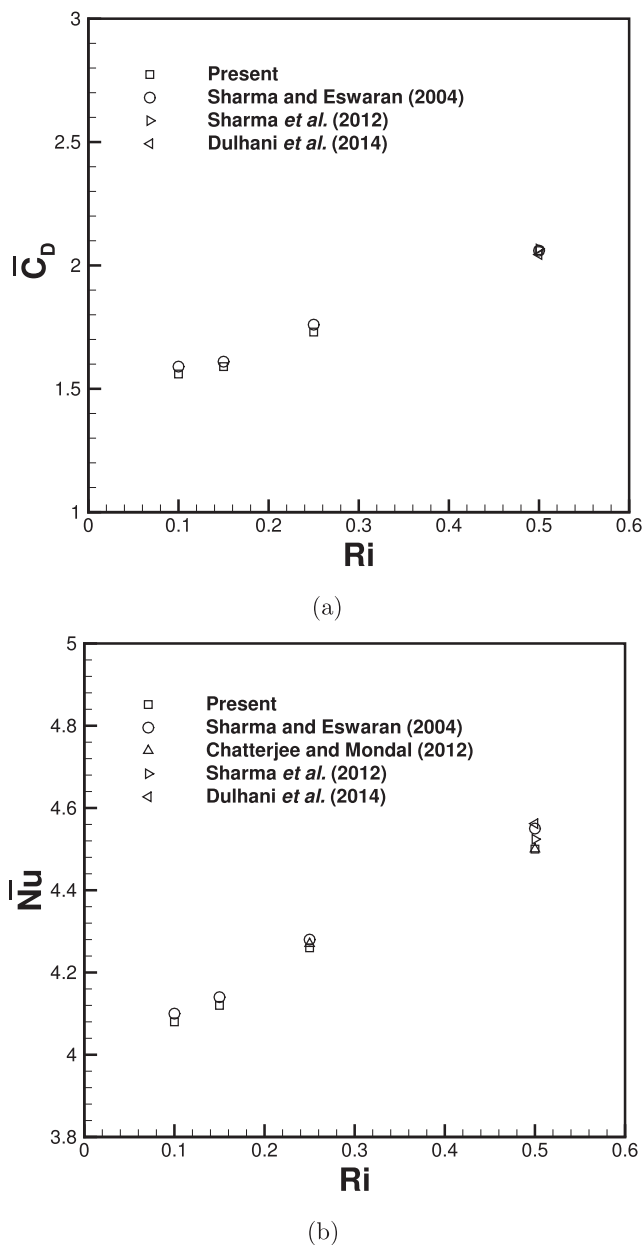


FIG. 5. Validation of the present code at different Richardson numbers for $\alpha = \phi = 0^\circ$, $Pr = 0.71$, and $Re = 100$.

IV. RESULTS AND DISCUSSION

Using a non-Boussinesq flow model, the role of thermal buoyancy in the vortex shedding suppression process is studied in detail for a 2D flow past a cylinder of the square cross section in the mixed convection regime. All computations are performed at $Re = 100$ and $M = 0.1$. The cylinder inclination, ϕ , is varied as $0 \leq \phi \leq 45^\circ$, the free-stream inclination, α , is varied as $0 \leq \alpha \leq 90^\circ$, and the over-heat ratio, ϵ , is varied as $0 \leq \epsilon$

≤ 2 . Two different Froude numbers, namely, $Fr = 1.0$ ($1/Fr^2 = 1.0$) and $Fr = 0.707$ ($1/Fr^2 = 2.0$) are considered.

A. Role of the Richardson number in controlling vortex shedding

It is well known that in small-scale heating scenarios modeled via OB approaches, the vortex shedding suppression process past a cylinder is governed by the non-dimensional parameter, the Richardson number defined as $Ri = g\beta\Delta Td/U_\infty^2$. For large-scale heating scenarios, as shown in Sec. III D, the scale or amount of heating is controlled by ϵ , while the ratio of inertia effects to gravitational effects is regulated by Fr . It is therefore of fundamental interest to identify the roles of (ϵ, Fr) or $Ri^{NB} = \frac{\epsilon}{Fr^2} \left(\frac{2}{2+\epsilon} \right)$ in vortex shedding suppression.

As explained in the work of Hasan and Ali,³² buoyancy force plays a central role in the suppression of vortex shedding from heated bluff-bodies in the mixed convective flow regime. A novel phenomenological model or mechanism of vortex shedding suppression was proposed by them that was well supported by the suppression characteristics observed from heated circular as well as square cylinders in 2D mixed convective flow regimes. However, since the study was based on the Boussinesq flow model, the suppression of vortex shedding was shown to be predominantly controlled by the Richardson number, Ri . It is reasonable to argue that even for large-scale heating in mixed convective flows, the mechanism of vortex shedding suppression by thermal buoyancy would fundamentally remain the same as proposed in the earlier work of Hasan and Ali.³² Therefore, one would like to examine the extent up to which vortex shedding suppression characteristics are correlated with the Richardson number, Ri^{NB} .

For this purpose, the simulations are performed at two different Froude numbers, $Fr_1 = 1.0$, $Fr_2 = 0.707$ ($1/Fr_1^2 = 1.0$, $1/Fr_2^2 = 2.0$). At these two Froude numbers, the critical over-heat ratio is determined for different inclinations, ϕ , of the cylinder. At any inclination, as the heating of the cylinder is increased, the thermal buoyancy increases which results in suppression of vortex shedding. The over-heat ratio at which the vortex shedding is suppressed completely is called critical over-heat ratio, ϵ_c . In order to determine ϵ_c , a series of numerical simulations are performed near the bifurcation or critical point. The critical overheat ratio is determined near the critical point using the Stuart-Landau^{32,46} theory. According to Stuart-Landau theory, the equilibrium amplitude A_e of oscillation in the flow field due to vortex shedding can be expressed in terms of critical over-heat ratio, ϵ_c , in the vicinity of the vortex shedding suppression point (bifurcation point) by a relation

$$A_e^2 = c_1(\epsilon - \epsilon_c). \quad (22)$$

Since the equilibrium amplitude decreases with the increase in ϵ and ultimately vanishes at $\epsilon = \epsilon_c$, the value of c_1 is negative. Using the $(A_e - \epsilon)$ data near the critical point, ϵ_c is determined for different angles of cylinder inclination at the two different Froude numbers. The equilibrium amplitude of the

lift coefficient is used as A_e .^{32,47–49} After obtaining the value of ϵ_c , the values of $\frac{\epsilon_c}{Fr^2} \left(\frac{2}{2+\epsilon_c} \right)$ and $\frac{\epsilon_c}{Fr^2} \left(\frac{2}{2+\epsilon_c} \right)$ obtained for different ϕ are plotted, as shown in Fig. 6. It shows that for small incidence angle (up to 20°) the two plots nearly coincide with each other. While for high incidence angles the two plots do not exactly coincide each other with a maximum deviation of nearly 27% for 45° incidence. The deviations in the values of $Ri_c^{NB} = \frac{\epsilon_c}{Fr^2} \left(\frac{2}{2+\epsilon_c} \right)$ at two different Froude numbers for higher incidence angles are due to the fact that at higher incidence angles more heating is required to suppress the vortex shedding since at high incidence angle stronger vortices are formed. At larger heating, the effect of variable transport properties (μ and κ) starts to play a significant role along with Ri_c^{NB} in suppression of vortex shedding.

This is a novel finding for mixed convective flows involving large scale heating or non-Boussinesq scenarios. The critical ϵ data for different values of ϕ at different Froude numbers can be made to collapse within a band of accuracy (2%–27%) using $Ri_c^{NB} = \frac{\epsilon_c}{Fr^2} \left(\frac{2}{2+\epsilon_c} \right)$ as the critical parameter. Figure 7 shows the streamline patterns before vortex shedding suppression and after vortex shedding suppression for three different orientations of the cylinder, i.e., $\phi = 0^\circ$, $\phi = 20^\circ$, and $\phi = 45^\circ$. The coefficient of the lift plot with time is also shown in Fig. 7 for the case when vortex shedding is present. When the vortex shedding is suppressed, then the amplitude of C_L vanishes. Hence, the time histories are not shown for the vortex shedding suppressed states.

The value of Ri_c^{NB} at which vortex shedding suppression occurs can be obtained at any inclination for $Fr = 1.0$ ($1/Fr^2 = 1.0$) by a cubic polynomial obtained by standard curve-fitting procedures given as

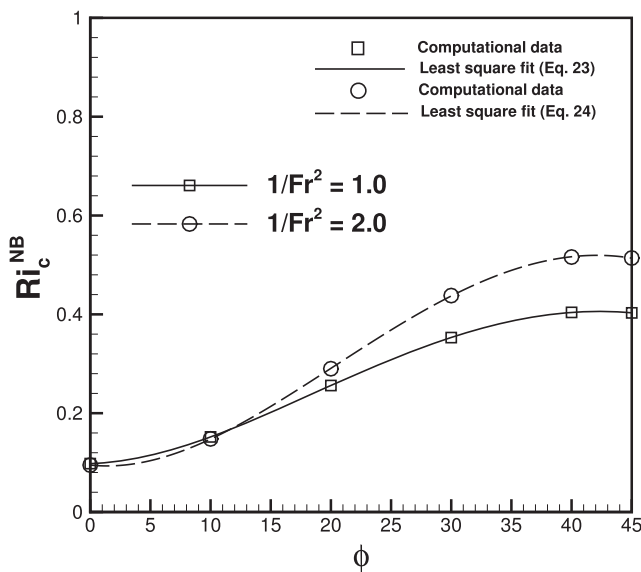


FIG. 6. Vortex shedding suppression characteristics at different Froude numbers in $(Ri_c^{NB}-\phi)$ space for $\alpha = 0^\circ$, $Pr = 0.71$, and $Re = 100$.

$$Ri_c^{NB} = B_0 + B_1\phi + B_2\phi^2 + B_3\phi^3 \quad (Fr = 1.0), \quad (23)$$

where ϕ is in degrees and the coefficients of the polynomial are given by $B_0 = 9.798 \times 10^{-2}$, $B_1 = 6.891 \times 10^{-4}$, $B_2 = 5.972 \times 10^{-4}$, and $B_3 = -1.313 \times 10^{-5}$ obtained by the least-square curve-fit approach. Similarly for $1/Fr^2 = 2.0$ or $Fr = 0.707$, the value of Ri_c^{NB} at which vortex shedding suppression occurs can be obtained at any inclination for $Fr = 0.707$ ($1/Fr^2 = 2.0$) by a polynomial given by

$$Ri_c^{NB} = C_0 + C_1\phi + C_2\phi^2 + C_3\phi^3 \quad (Fr = 0.707), \quad (24)$$

where ϕ is in degrees and the coefficients of the polynomial are given by $C_0 = 9.507 \times 10^{-2}$, $C_1 = -2.588 \times 10^{-3}$, $C_2 = 9.647 \times 10^{-4}$, and $C_3 = -1.87 \times 10^{-5}$ obtained by the least-square curve-fit approach. The correlations proposed in Eqs. (23) and (24) are shown by solid and dashed line, respectively, while the computational data are shown by square and circle symbols, respectively, in Fig. 6. It is very much evident that the curve-fits capture the computational data trends quite accurately.

B. Neutral curves in the parametric space of $\epsilon-\phi$ and $\epsilon-\alpha$ for $Fr = 1.0$

In this subsection, the effect of cylinder inclination as well as free-stream inclination on the process of vortex shedding suppression by heating is studied in detail. It has already been shown that when heating is large, the vortex shedding suppression is not solely controlled by buoyancy of Ri_c^{NB} .

In the mixed convection regime, both cylinder inclination and free-stream orientation act as independent parameters that affect the vortex shedding suppression phenomena. As the inclination of the cylinder is altered, the flow dynamics past a square cylinder also changes. The effect of cylinder inclination on the vortex shedding is already discussed in Sec. IV A by keeping the free-stream orientation fixed (i.e., $\alpha = 0^\circ$). Figure 8 shows the plot of the critical over-heat ratio, ϵ_c with cylinder inclination, ϕ . This plot is the neutral curve which separates the steady flows from unsteady flows in $\epsilon-\phi$ parametric space for $Fr = 1.0$. It is observed that with an increase in ϕ , the critical ϵ increases up to $\phi = 40^\circ$ and shows a slight decrease for $\phi = 45^\circ$.

The value of ϵ_c at which vortex shedding suppression occurs can be obtained at any inclination for $Fr = 1.0$ via a polynomial given as

$$\epsilon_c = D_0 + D_1\phi + D_2\phi^2 + D_3\phi^3 \quad (Fr = 1.0), \quad (25)$$

where ϕ is in degrees and the coefficients of the polynomial are given by $D_0 = 1.030 \times 10^{-1}$, $D_1 = 6.192 \times 10^{-4}$, $D_2 = 6.557 \times 10^{-4}$, and $D_3 = -1.054 \times 10^{-5}$ obtained by the least-square curve-fit approach. The curve-fit relation given in Eq. (25) is shown by solid line, while the computational data are shown by square symbols in Fig. 8.

In order to quantify and segregate the effects of large-scale heating regulating the vortex shedding suppression, as captured by the present NOB model, a similar neutral curve is also obtained using a conventional Boussinesq model with $Ri = \epsilon/Fr^2$ as the classical buoyancy to inertial effect

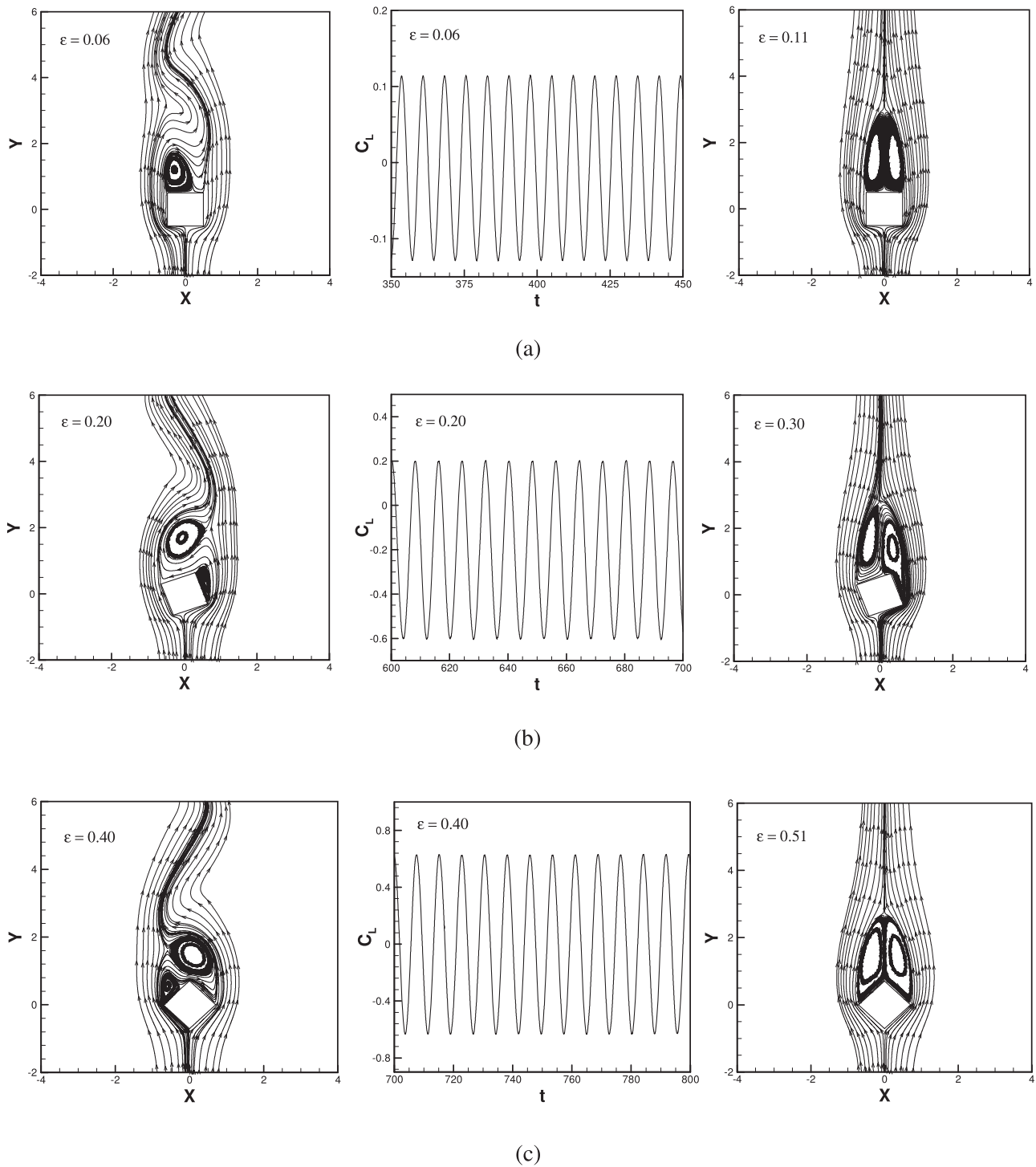


FIG. 7. Patterns before and after suppression for the NOB model at (a) $\phi = 0^\circ$, (b) $\phi = 20^\circ$, and (c) $\phi = 45^\circ$. The flow parameters are kept as $\alpha = 0^\circ$, $Pr = 0.71$, $Fr = 1.0$, and $Re = 100$.

parameters. Since the data obtained from the NOB model are at $Fr = 1.0$, the simulations employing the Boussinesq model have been carried out by setting $Ri = \epsilon$. Hence the critical ϵ_c

can be compared to the OB model data for Ri_c , as shown in Fig. 8. The critical Ri for the OB model have been obtained by carrying out simulations on identical numerical parameters

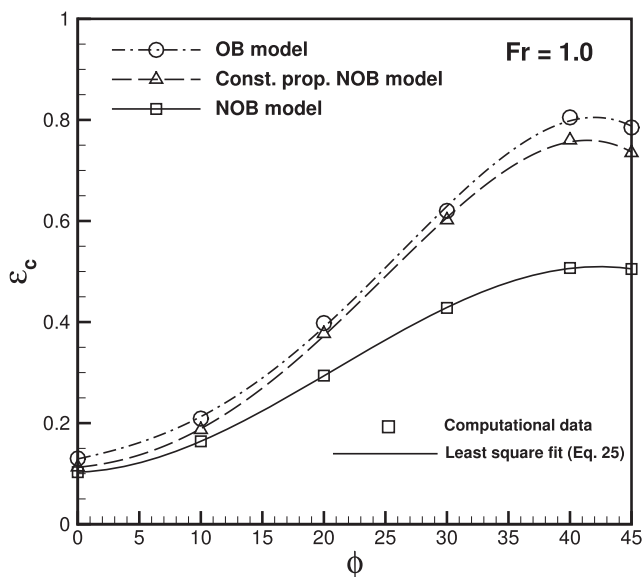


FIG. 8. Neutral curves in $(\epsilon_c - \phi)$ space at flow parameters of $\alpha = 0^\circ$, $Fr = 1.0$, $Pr = 0.71$, and $Re = 100$. These curves separate the steady and unsteady flow regimes for different models.

like grid size and distance of far boundary, using an in-house structured body-fitted computer code employing the Simplified Marker and Cell (SMAC) type scheme.³² It is readily observed from Fig. 8 that except for very low ϕ ($\phi < 10^\circ$), the vortex shedding suppression characteristics as captured by the NOB model are significantly deviated from those obtained by the OB model for same ϕ . In fact for large-scale heating scenario, ϵ_c is significantly lower. It is reasonable to argue that for the NOB model, the effects of increase in viscosity and thermal conductivity in the wake and in the neighborhood of the cylinder, in general, would enhance the stability of the wake. This would aid the buoyancy effects in bringing about suppression of vortex shedding, resulting in lower values of ϵ_c .

This is further supported by the findings of Hasan and Saeed²⁴ where, using the present NOB model, an increase in ϵ_c , even for a forced convective flow regime, was shown to reduce oscillations in the flow due to vortex shedding and even caused vortex shedding suppression for very large heating ($\epsilon_c \sim 1.0$), in the absence of buoyancy effects.

In order to examine the extent of the role played by an increase in molecular transport properties towards causing suppression of vortex shedding, simulations are also carried out with the present NOB model with molecular transport properties deliberately maintained constant, i.e. ($\mu = \kappa = 1.0$). The dashed line in Fig. 8 represents the critical ϵ_c obtained for different cylinder orientations using this approach. Interestingly the vortex shedding suppression characteristics obtained from a constant property non-Boussinesq model are quite close for those recovered from a Boussinesq model ($\epsilon_c = Ri_c$) for a small-scale heating scenario. This is another key finding of the present study. The effects of volumetric

straining and associated compression work do not affect the vortex shedding suppression phenomenon very significantly. It is therefore concluded that it is necessary to account for effects of variations in molecular transport properties under large-scale heating situation in order to accurately capture the vortex shedding suppression phenomena for mixed convective flows past heated bluff bodies.

It is also worth pointing out that slight deviations in the constant property NOB model predictions of the critical values of ϵ_c can be attributed to finite volumetric straining effects as opposed to Boussinesq model predictions that involve a limiting incompressible (volumetric strains or $\nabla \cdot \vec{V} = 0$) flow scenario.

Figure 8 also depicts a striking qualitative resemblance in the three neutral curves obtained from Boussinesq as well as the two NOB models. This suggests that the fundamental mechanism of vortex shedding suppression, as proposed by Hasan and Ali³² and supported by their numerical data obtained via the Boussinesq model, is likely to be same in the scenario of the non-Boussinesq mixed convective flow regime.

The increase in ϕ up to nearly 40° causes critical ϵ_c to increase monotonically. This is primarily due to the increase in asymmetry in the wake flow structure as ϕ is increased, thereby requiring higher levels of heating to cause suppression in vortex shedding. The values of critical ϵ_c are somewhat lower for $\phi = 45^\circ$ in comparison to those corresponding to $\phi = 40^\circ$ (Fig. 8). This is because at $\phi = 45^\circ$, the flow structure of the counter rotating vortices evolves symmetrically and any instability that has a tendency to break the symmetry is suppressed by buoyancy effects at lower levels of heating. This is confirmed by the mean streamline patterns drawn for the unsteady state just before suppression of vortex shedding in Fig. 9 for cylinder inclinations $\phi = 40^\circ$ and $\phi = 45^\circ$.

The effect of specific heat on the vortex shedding suppression characteristics or the neutral curve is also studied. In this case, the simulations are performed (using the same NOB code but with constant specific heat only) at cylinder inclination of $\phi = 40^\circ$ since maximum deviation of critical parameter is seen at $\phi = 40^\circ$. The critical over-heat ratio ϵ_c (at $Fr = 1.0$) is found to be 0.552 using the same procedure as discussed in Sec. IV A. While the value of ϵ_c for the full NOB model (variable specific heat and transport properties) is found to be $\epsilon_c = 0.507$. This shows that the deviation of ϵ_c for the constant specific heat NOB model from the full NOB model is very less (nearly 8.2%). On the other hand at $\phi = 40^\circ$, the constant transport property NOB model predicts $\epsilon_c = 0.76$. Comparing this to the full NOB model prediction, the deviation is nearly 37.7%. This shows that along with buoyancy the temperature dependent transport properties play a dominating role in the vortex shedding suppression characteristics as compared to volumetric straining effects and specific heat variations.

The deviations observed in the vortex shedding suppression characteristics between various NOB models and the OB model at $Re = 100$ are expected to follow a similar trend even for other Re of comparable order. In order to examine this,

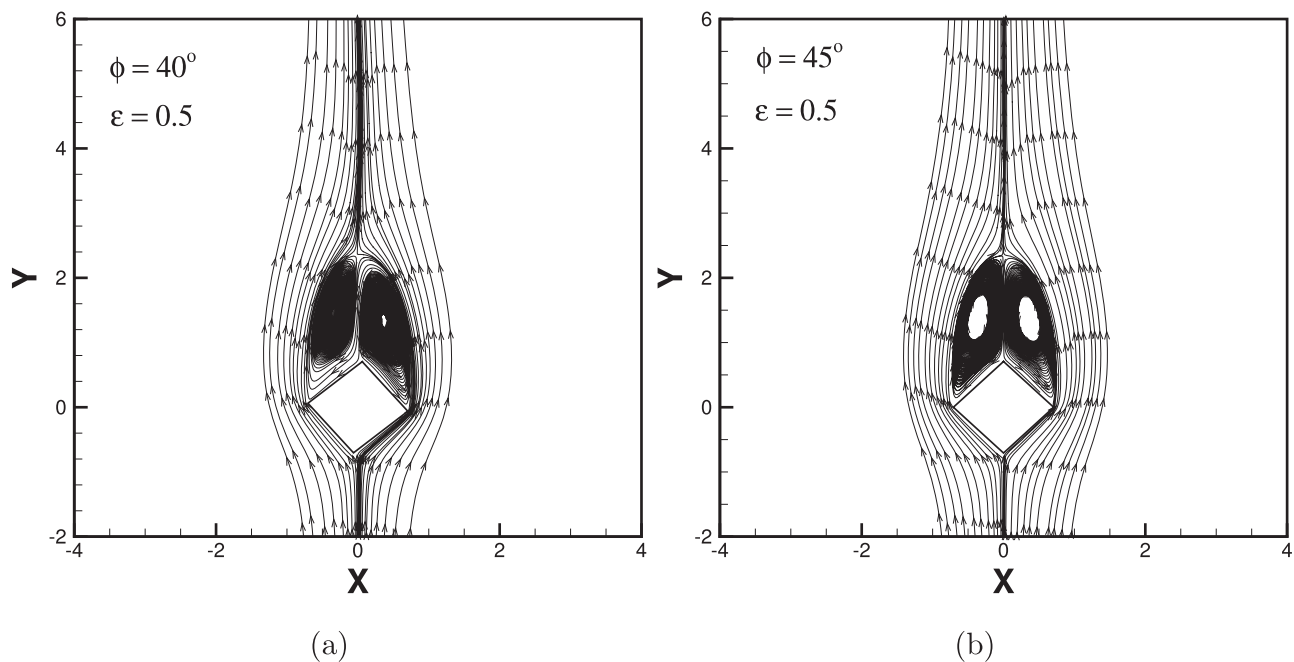


FIG. 9. Mean flow structure in wake for the NOB model at (a) $\phi = 40^\circ$ and (b) $\phi = 45^\circ$. The flow parameters are kept as $\alpha = 0^\circ$, $Fr = 1.0$, $Pr = 0.71$, and $Re = 100$.

numerical computations are carried out at $Re = 130$ with other parameters given as $\alpha = 0^\circ$, $\phi = 40^\circ$, $Fr = 1.0$, and $Pr = 0.71$. Table VI compares the values of ϵ_c (critical overhear ratio) for different NOB models with the OB model. The values clearly indicate a negligible effect of specific heat variations and strong effect of transport property variations at $Re = 130$. Computations at much higher Re have not been considered owing to the possibility of onset of three-dimensionality in the wake that is outside the scope of current two-dimensional investigation.

Free-stream inclination effects on the vortex shedding suppression process are also presented in this subsection. It is known that the flow dynamics is also affected by changing the free-stream inclination. In most of the earlier studies, the free-stream inclination was either, $\alpha = 0^\circ$ (aligned flow) or $\alpha = 90^\circ$ (cross flow). Only in the recent studies of Hasan and Ali³² the free-stream inclination was varied as $0 \leq \alpha \leq 90^\circ$. Using the OB model, they identified the neutral curve which separates the steady flows from unsteady flows in the small-scale heating regimes in the Ri - α parametric space. The present work also aims to identify the neutral curves separating the steady and unsteady flow past a square

cylinder for a large-scale heating regime in the ϵ_c - α parametric space. In order to determine this, a series of numerical simulations are performed at each free-stream inclination ($Fr = 1.0$) near the bifurcation or critical point, and using equilibrium C_L amplitudes and Stuart Landau theory the critical over-heat ratio is determined. The neutral curve ($\epsilon_c = f(\alpha)$) obtained by a curve fitting a cubic polynomial relation is given as

$$\epsilon_c = E_0 + E_1\alpha + E_2\alpha^2 + E_3\alpha^3 \quad (Fr = 1.0), \quad (26)$$

where α is in degree, and the coefficients of the polynomial are given as $E_0 = 1.035 \times 10^{-1}$, $E_1 = -3.183 \times 10^{-3}$, $E_2 = 1.279 \times 10^{-3}$, and $E_3 = -2.883 \times 10^{-5}$. The computational data (shown by square symbol) in Fig. 10 match quite well with the proposed correlation in Eq. (26) shown by solid line.

The values of critical buoyancy parameters for both OB and NOB models are compared in Fig. 10. The data for the critical Richardson number ($\epsilon_c = Ri_c$) at different free-stream orientations for the OB model is taken from Ref. 32. Since $Fr = 1.0$, for OB models $Ri = \epsilon$. The neutral curves for both the models show a similar trend (non-monotonic trend). Figure 10 shows that for the NOB model the vortex shedding suppression does not take place for free-stream orientations, $\alpha \geq 80^\circ$ for the range of ϵ depicted in the figure. In fact, an increase in ϵ up to 2 also did not cause suppression of vortex shedding for $\alpha \geq 80^\circ$. This is in conformance with the absence of vortex shedding suppression in cross flow ($\alpha = 90^\circ$) as reported by Bhattacharyya and Mahapatra,²⁸ employing an OB model. This is also in conformance with the phenomenological model given by Hasan and Ali,³² highlighting the role of baroclinic

TABLE VI. Comparison of ϵ_c for various NOB models with the OB model at $Re = 130$.

NOB model	Constant specific heat model	Constant transport property model	OB model
0.70	0.75	1.20	1.28

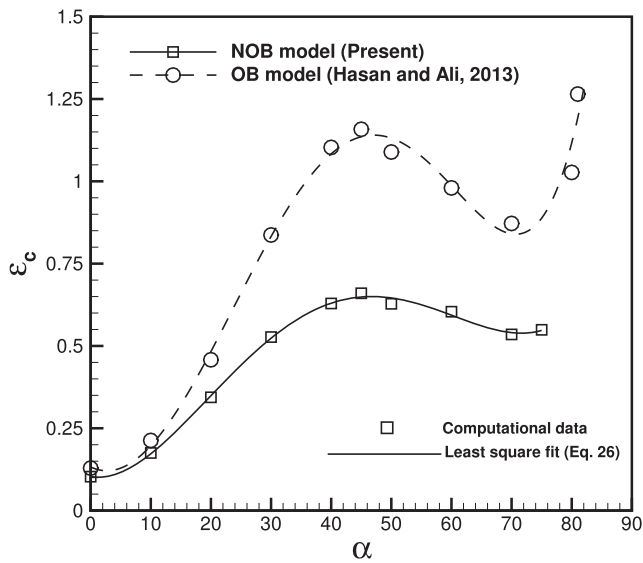


FIG. 10. Neutral curves in $(\epsilon-\alpha)$ space for OB and NOB models at $\phi = 0^\circ$, $Fr = 1.0$, $Pr = 0.71$, and $Re = 100$. These curves separate the steady and unsteady flow regimes.

vorticity in vortex shedding suppression characteristics. From Fig. 10, it is also observed that for small α (up to $\alpha = 20^\circ$) the neutral curves for both models show less deviation from each other. But for $\alpha > 20^\circ$ there is a significant deviation of critical parameters between both models. The reason behind this is that at small α ($\alpha < 20^\circ$) low heating is required for suppression of vortex shedding, while at large α more heating is required for suppression of vortex shedding. For a small heating regime, the effects of thermal straining and variation in transport properties are negligible and suppression of vortex shedding is primarily caused by buoyancy, as captured identically by both models.

C. Vorticity dynamics in wake and vortex shedding suppression

In the present section, the vorticity dynamics in the near wake and the mechanism behind the suppression of vortex shedding by thermal effects in the large-scale heating scenario or non-Boussinesq scenario is investigated. For this, the X and Y components of momentum equations are used. If these equations [Eqs. (3) and (4)] are expressed in non-conservative form, one obtains

$$\frac{\partial \vec{V}}{\partial t} = -\frac{\nabla p}{\rho} + \frac{(1-\rho)}{\rho Fr^2} \hat{j} + \frac{1}{\rho} (\nabla \cdot \overline{\overline{\sigma}}^v). \quad (27)$$

This can be further written as

$$\frac{D\vec{V}}{Dt} + \nabla \left(\frac{V^2}{2} \right) + \Omega \times \vec{V} = -\frac{\nabla p}{\rho} + \frac{(1-\rho)}{\rho Fr^2} \hat{j} + \frac{1}{\rho} (\nabla \cdot \overline{\overline{\sigma}}^v). \quad (28)$$

Taking curl of this momentum equation, one can obtain the vorticity transport equation as

$$\begin{aligned} \frac{D\vec{\Omega}}{Dt} &= (\vec{\Omega} \cdot \nabla) \vec{V} - (\nabla \cdot \vec{V}) \vec{\Omega} + \nabla \\ &\times \left[-\frac{\nabla p}{\rho} + \frac{1}{Fr^2} \frac{(1-\rho)}{\rho} \hat{j} \right] + \nabla \times \frac{1}{\rho} (\nabla \cdot \overline{\overline{\sigma}}^v). \end{aligned} \quad (29)$$

For 2D flows, the vortex stretching term $(\vec{\Omega} \cdot \nabla) \vec{V} = 0$,

$$\frac{D\vec{\Omega}}{Dt} = -(\nabla \cdot \vec{V}) \vec{\Omega} + \frac{1}{\rho^2} \left[\nabla \rho \times \nabla p - \frac{1}{Fr^2} \frac{\partial \rho}{\partial x} \hat{k} \right] + \nabla \times \frac{1}{\rho} (\nabla \cdot \overline{\overline{\sigma}}^v). \quad (30)$$

The baroclinic contribution to vorticity is given as

$$\frac{D\vec{\Omega}^b}{Dt} = \frac{1}{\rho^2} \left[\nabla \rho \times \nabla p - \frac{1}{Fr^2} \frac{\partial \rho}{\partial x} \hat{k} \right]. \quad (31)$$

From Eq. (8), we have,

$$(\rho T - 1) = \gamma M^2 p. \quad (32)$$

Taking grad on both sides, Eq. (32) becomes

$$T \nabla \rho + \rho \nabla T = \gamma M^2 \nabla p. \quad (33)$$

Furthermore,

$$\nabla \rho \times [T \nabla \rho + \rho \nabla T] = \gamma M^2 \nabla \rho \times \nabla p. \quad (34)$$

After, further simplification we get

$$\nabla \rho \times \nabla p = \frac{\nabla \rho \times \rho \nabla T}{\gamma M^2}. \quad (35)$$

Thus, Eq. (31) can be expressed as

$$\left[\frac{D\vec{\Omega}^{(b)}}{Dt} \right]_{prod.} = \frac{1}{\rho^2} \left[\frac{1}{\gamma M^2} |\nabla \rho \times \rho \nabla T| \hat{k} - \frac{1}{Fr^2} \frac{\partial \rho}{\partial x} \hat{k} \right]. \quad (36)$$

In the limit of a small Mach number (M), $\rho \approx 1/T$. Thus, $\nabla \rho$ is nearly parallel to ∇T , which implies that $\nabla \rho$ is also nearly parallel to $\rho \nabla T$. This implies that $\nabla \rho \times \rho \nabla T$ would be quite small in the wake and can be neglected. Thus Eq. (36) simplifies to

$$\left[\frac{D\vec{\Omega}^{(b)}}{Dt} \right]_{prod.} \approx -\frac{1}{Fr^2} \frac{1}{\rho^2} \frac{\partial \rho}{\partial x} \hat{k} \quad (37)$$

or

$$\left[\frac{D\vec{\Omega}^{(b)}}{Dt} \right]_{prod.} \approx -\frac{1}{Fr^2} \frac{1}{\rho^2} \frac{\partial \rho}{\partial x}; \text{ since } \vec{\Omega}^{(b)} = \Omega^{(b)} \hat{k}. \quad (38)$$

Figure 11 shows a typical sketch showing the wake and the local n-s coordinate system used to analyze the density gradients and the volumetric strains across the interface of counter rotating vortices. At fixed y,

$$\frac{\partial n}{\partial x} = \cos \alpha; \quad \frac{\partial s}{\partial x} = \sin \alpha. \quad (39)$$

Thus, Eq. (37) transform into

$$\left[\frac{D\vec{\Omega}^{(b)}}{Dt} \right]_{prod.} = -\frac{1}{Fr^2} \frac{1}{\rho^2} \left[\frac{\partial \rho}{\partial n} \cos \alpha + \frac{\partial \rho}{\partial s} \sin \alpha \right]. \quad (40)$$

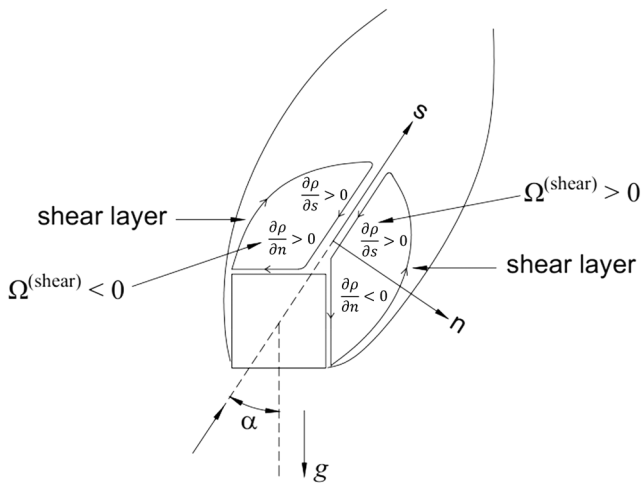
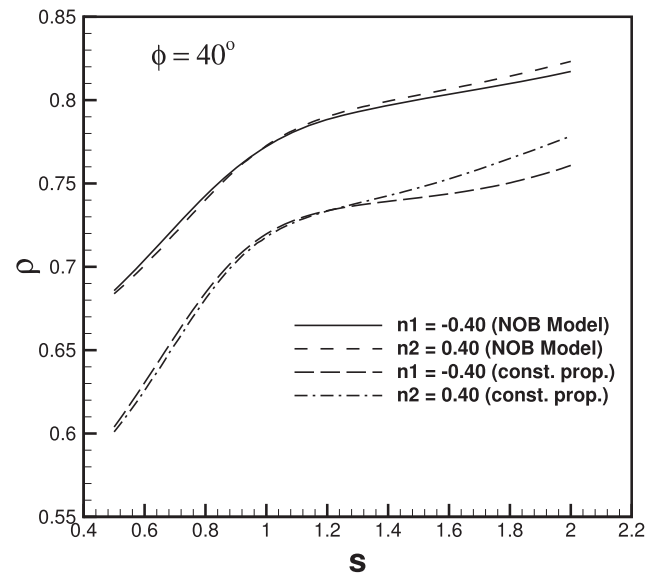


FIG. 11. Schematic diagram showing the vortices in the critical state with (n-s) co-ordinates.

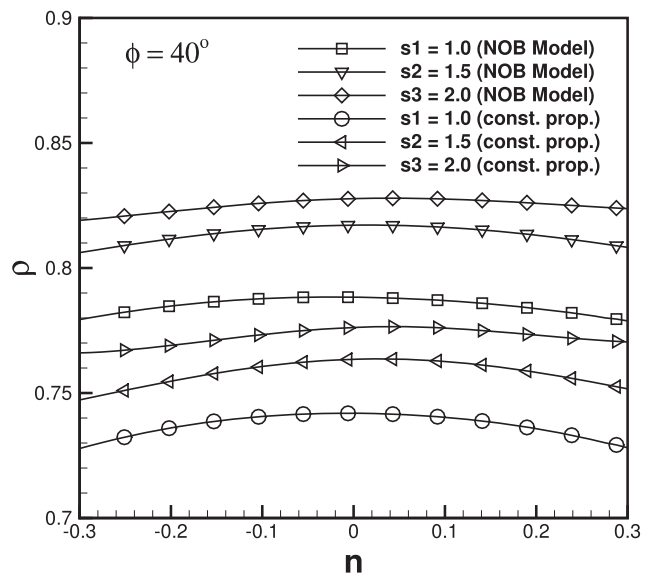
Figure 12 shows the density variations with respect to the coordinates (s-n) for ($\alpha = 0^\circ$, $\phi = 40^\circ$, $\epsilon = 0.51$). Since $\alpha = 0^\circ$, directions n and s coincide with directions of x and y, respectively. Now from Fig. 12(a), $\frac{\partial \rho}{\partial s} > 0$ for both $n > 0$ and $n < 0$. Thus in wake $-\frac{1}{Fr^2 \rho^2} \frac{\partial \rho}{\partial s} \sin \alpha$ is negative or generates negative vorticity only. Following the phenomenological arguments of Hasan and Ali,³² such a vorticity producing term alone cannot cause suppression of vortex shedding as it promotes asymmetry in the counter rotating vortices. Analyzing the vorticity production contribution of the other term $-\frac{1}{Fr^2 \rho^2} \frac{\partial \rho}{\partial n} \cos \alpha$, we have from Fig. 12(b), $\frac{\partial \rho}{\partial n} > 0$ for $n < 0$ and $\frac{\partial \rho}{\partial n} < 0$ for $n > 0$. Thus, as shown in Fig. 11, this term generates negative and positive vorticities in harmony with the sense of vorticity induced by the separating shear layers on the left and right sides of the interface of the vortices, respectively. Hence this is the only symmetry preserving (in terms of sense of vorticity) component of $\frac{D\Omega^{(b)}}{Dt}$. Thus, it is the presence of the baroclinic vorticity production term $-\frac{1}{Fr^2 \rho^2} \frac{\partial \rho}{\partial n} \cos \alpha$ that leads to vortex shedding suppression. However since the non-symmetry preserving term $-\frac{1}{Fr^2 \rho^2} \frac{\partial \rho}{\partial s} \sin \alpha$ is also present, the steady wakes observed after suppression of vortex shedding are somewhat asymmetric for different α .

Figure 13 shows the variation of vorticity and density in the wake for the two steady cases ($\alpha = 0^\circ$, $\phi = 10^\circ$, $\epsilon = 0.17$) and ($\alpha = 0^\circ$, $\phi = 40^\circ$, $\epsilon = 0.51$). It is worth noting that in the steady wakes, the vorticity variations across the interface are symmetric, while the density gradients that bring about suppression are asymmetric.

In the vorticity transport equations, in addition to the baroclinic term $\frac{D\Omega^{(b)}}{Dt}$ the other vorticity production or source term is $-(\nabla \cdot \vec{V})\vec{\Omega}$. This term physically represents the effect of volumetric straining on vorticity generation. For further references and arguments, we refer to it as a volumetric straining



(a)



(b)

FIG. 12. (a) Variation of density with s at two different values of n. (b) Variation of density with n at three different values of s for $\alpha = 0^\circ$, $Fr = 1.0$, $Pr = 0.71$, and $Re = 100$. These plots are at ϵ just greater than ϵ_c .

vorticity generation rate $\frac{D\vec{\Omega}^{(vs)}}{Dt} = -(\nabla \cdot \vec{V})\vec{\Omega} = -(\nabla \cdot \vec{V})\Omega \hat{k}$. This term is negligible for small scale heating scenarios and therefore is neglected in Boussinesq models. Analysis of the role of $-(\nabla \cdot \vec{V})\Omega \hat{k}$, if any, in vortex shedding suppression is also a novel contribution of the present work.

Figure 14 shows the variation of $(\nabla \cdot \vec{V})$ or dilatation rate at several distances “s” in the wake for ($\alpha = 0^\circ$, $\phi = 40^\circ$, $\epsilon = 0.51$).

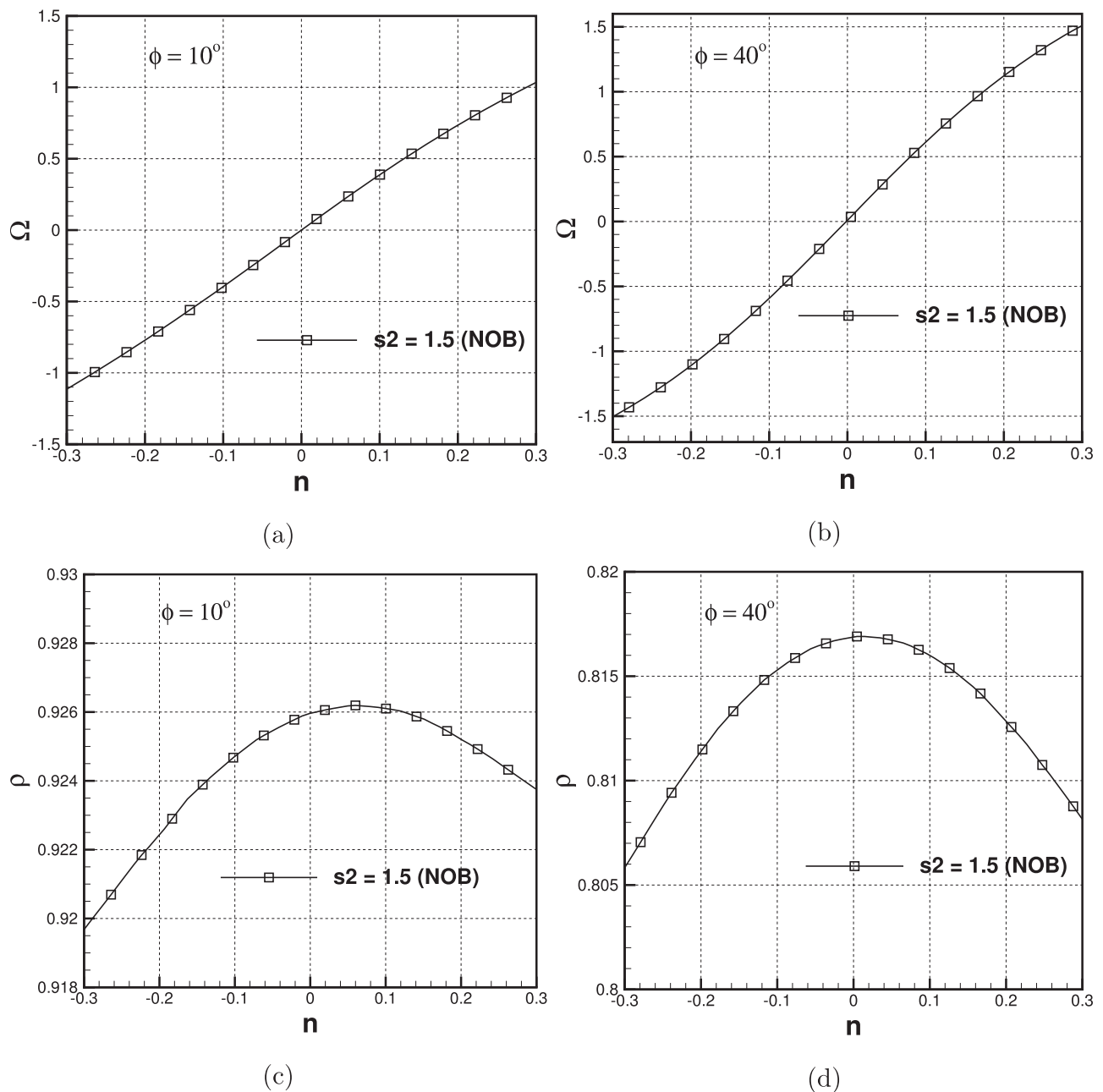


FIG. 13. Variation of vorticity with n at $s2 = 1.5$ for (a) $\phi = 10^\circ$ and (b) $\phi = 40^\circ$. Variation of density with n at $s2 = 1.5$ for (c) $\phi = 10^\circ$ and (d) $\phi = 40^\circ$. The flow parameters are $\alpha = 0^\circ$, $Fr = 1.0$, $Pr = 0.71$, and $Re = 100$. These plots are at ϵ just greater than ϵ_c .

The distances are measured from the cylinder centre. The variation indicates that the values are significant near the cylinder and progressively reduce moving away from the cylinder. It is to be observed that values on either side of the interface of vortices ($n = 0$) are positive. From the earlier Fig. 13, for $n < 0$, $\Omega < 0$ while for $n > 0$, $\Omega > 0$. This implies

that $\frac{D\Omega^{(VS)}}{Dt} = -(\nabla \cdot \vec{V})\Omega > 0$ for $n < 0$ and $-(\nabla \cdot \vec{V})\Omega < 0$ for $n > 0$ in the neighbourhood of the interface. Thus, the action of the term $-(\nabla \cdot \vec{V})\Omega$ on either side of the interface of vortices is to *reduce* the base vorticity present in left and right vortices as fed from the shear layers. Hence this term directly has a symmetry preserving effect on the vorticity associated

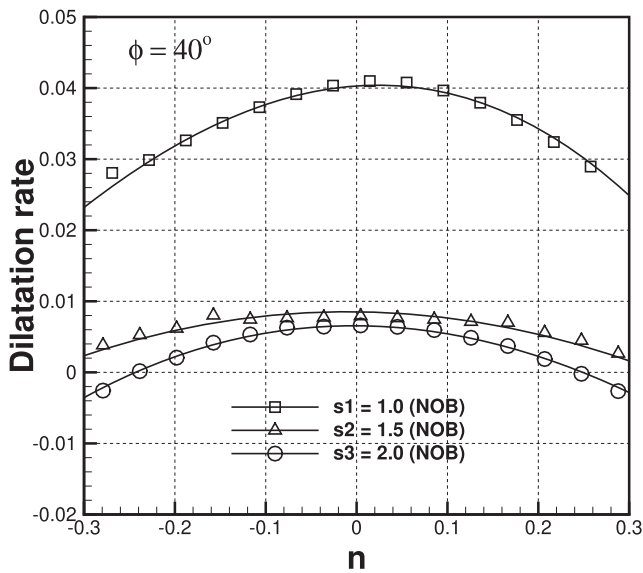


FIG. 14. Variation of dilatation rate with n at different values of s for $\alpha = 0^\circ$, $\phi = 40^\circ$, $\epsilon = 0.51$, $Fr = 1.0$, $Pr = 0.71$, and $Re = 100$. These plots are at ϵ just greater than ϵ_c .

with the twin counter rotating vortices. Thus it is shown that $-\frac{1}{Fr^2} \frac{1}{\rho^2} \frac{\partial \rho}{\partial n} \cos \alpha$ and $-(\nabla \cdot \vec{V})\Omega$ both have a symmetry preserving character as far as vorticity distribution on either side of the interface of vortices is concerned.

In the event of any perturbation causing a loss of symmetry in vorticity distribution across the interface of vortices, both the terms $-(\nabla \cdot \vec{V})\Omega$ and $-\frac{1}{Fr^2} \frac{1}{\rho^2} \frac{\partial \rho}{\partial n} \cos \alpha$ tend to reduce the imbalance or have a symmetry restoring character. If the negative vorticity ($n < 0$) builds up more than positive vorticity on the side ($n > 0$), then the imbalance would reduce as there would be more reduction on higher negative vorticity side ($n < 0$) than the reduction on the positive vorticity side ($n > 0$).

A similar effect is associated with the baroclinic component $-\frac{1}{Fr^2} \frac{1}{\rho^2} \frac{\partial \rho}{\partial n} \cos \alpha$. If the negative vorticity on side ($n < 0$) increases in magnitude in comparison to positive vorticity on ($n > 0$), then owing to a higher rate of mixing caused by higher vorticities, the thermal stratification or $\frac{\partial \rho}{\partial n}$ for $n < 0$ is reduced. This leads to a lower baroclinic vorticity generation on the higher vorticity side of the interface in comparison to the lower vorticity side, thereby reducing the imbalance. Due to the combined symmetry restoring effects of the baroclinic component and volumetric straining component, the vorticity magnitudes $|\Omega|$, across the interface $n = 0$ shown in Fig. 13, are nearly symmetric.

The combined effects of $\frac{D\Omega^{(VS)}}{Dt} = -(\nabla \cdot \vec{V})\Omega$ and $(-\frac{1}{Fr^2} \frac{1}{\rho^2} \frac{\partial \rho}{\partial n} \cos \alpha)$ are thus shown to be symmetry preserving and also symmetry restoring that eventually lead to suppression of vortex shedding in the large-scale heating scenario. The variation in transport properties (μ, k) also plays

a significant role in assisting the baroclinic and volumetric straining vorticity production effects. An increase in (μ, k) due to heating enhances the molecular diffusion rates of momentum and heat resulting in lower effective Reynolds and Peclet Pe ($= RePr$) numbers in the flow field near the heated cylinder. The lowering of effective Re and Pe has a stabilizing effect on the vortex shedding instability which is generally known to be promoted with an increase in Re . In comparison to the roles of baroclinic vorticity and temperature dependent molecular transport properties, however, the role of $-(\nabla \cdot \vec{V})\Omega$ or thermal straining vorticity production is somewhat weak but noticeable as can be ascertained from Fig. 8, where ϵ_c for the constant transport property NOB model is only slightly lower than that for the OB model at different ϕ .

To conclude, in the large-scale heating scenario, the vortex shedding suppression characteristics are controlled by

- ratio of inertia to buoyancy forces or $Ri^{NB} = \frac{\epsilon}{Fr^2} \left(\frac{2}{2+\epsilon} \right)$,
- the effects of thermal straining vorticity production $-(\nabla \cdot \vec{V})\Omega$, and
- temperature dependence of molecular transport properties of the fluid.

Based on these arguments, in the limit of small heating, it can be argued that vortex shedding suppression is solely caused by baroclinic vorticity production. The neutral curve for $\alpha = 0^\circ$ (Ri^{NB} Vs ϕ), shown in Fig. 6, confirms this for $\phi < 20^\circ$ for which $\epsilon_c < 0.3$.

The neutral curve at $Fr = 1.0$ of ϵ_c vs α (shown in Fig. 10) bears a striking qualitative resemblance with the data obtained from a Boussinesq model. This can be explained from the phenomenological model of vortex shedding suppression given above for the class of flow under consideration. The vortex shedding would be suppressed when

$$\int_{wake} \left[\frac{D\Omega^{(b)}}{Dt} \right]_{prod.} dA \simeq \frac{1}{Fr^2} \int_{wake} \left[-\frac{1}{\rho^2} \frac{\partial \rho}{\partial n} \cos \alpha - \frac{1}{\rho^2} \frac{\partial \rho}{\partial s} \sin \alpha \right] dA$$

attains a threshold value represented symbolically as $\left[\frac{D\Omega^{(b)}}{Dt} \right]_{Th.}$ in the parametric space of α for fixed values of ϕ , Re , Pr , and Fr . This is assuming a weak effect of the term $-(\nabla \cdot \vec{V})\Omega$. Since for weakly compressible flows, $\rho \simeq 1/T$ and hence $\frac{1}{\rho^2} \frac{\partial \rho}{\partial n} = -\frac{\partial T}{\partial n}$; $\frac{1}{\rho^2} \frac{\partial \rho}{\partial s} = -\frac{\partial T}{\partial s}$, we have

$$\int_{wake} \left[\frac{D\Omega^{(b)}}{Dt} \right]_{prod.} dA \simeq \frac{1}{Fr^2} \int_{wake} \left[\frac{\partial T}{\partial n} \cos \alpha + \frac{\partial T}{\partial s} \sin \alpha \right] dA. \quad (41)$$

It can be shown that temperature gradients in the cylinder wake and the integrals $\int_{wake} \frac{\partial T}{\partial n} dA$, $\int_{wake} \frac{\partial T}{\partial s} dA$ scale as ϵ . Figure 15 shows the variation of $\int_{wake} |\nabla T| dA$ with over-heat ratio for the case of $\alpha = \phi = 0$. A perfect linear plot for $0.2 \leq \epsilon \leq 1.0$ confirms the scaling arguments. Therefore,

$$\int_{wake} \left(\frac{\partial T}{\partial n}, \frac{\partial T}{\partial s} \right) dA = \epsilon \int_{wake} \left(\left(\frac{\partial T}{\partial n} \right)_{scaled}, \left(\frac{\partial T}{\partial s} \right)_{scaled} \right) dA. \quad (42)$$

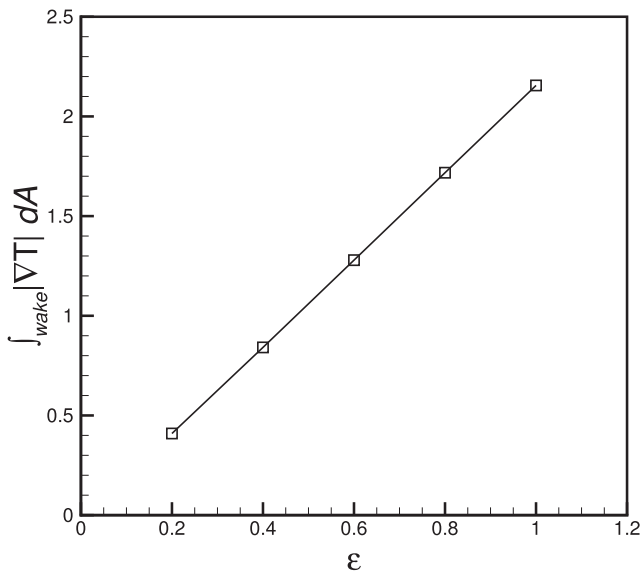


FIG. 15. Variation of $\int_{wake} |\nabla T| dA$ with ϵ for $\alpha = \phi = 0$, $Fr = 1.0$, $Pr = 0.71$, and $Re = 100$.

Equation (41) may re-expressed as

$$\int_{wake} \left[\frac{D\Omega^{(b)}}{Dt} \right]_{prod.} dA \approx \frac{\epsilon}{Fr^2} \left[\left(\int \left(\frac{\partial T}{\partial n} \right)_{scaled} dA \right) \cos \alpha + \left(\int \left(\frac{\partial T}{\partial s} \right)_{scaled} dA \right) \sin \alpha \right]. \quad (43)$$

As shown earlier that $\left(\int \left(\frac{\partial T}{\partial n} \right)_{scaled} dA \right)$ and $\left(\int \left(\frac{\partial T}{\partial s} \right)_{scaled} dA \right)$ are functions of α only for fixed (ϕ , Re , Pr , and Fr), while $\left(\int_{wake} \left[\frac{D\Omega^{(b)}}{Dt} \right]_{prod.} dA \right)$ is also a function of α . Thus, symbolically the integrals in Eq. (43) may be written as

$$\begin{aligned} \int_{wake} \left[\frac{D\Omega^{(b)}}{Dt} \right]_{Th.} dA &= h_1(\alpha), \\ \int \left(\frac{\partial T}{\partial n} \right)_{scaled} dA &= h_2(\alpha), \\ \int \left(\frac{\partial T}{\partial s} \right)_{scaled} dA &= h_3(\alpha). \end{aligned} \quad (44)$$

Hence the critical over-heat ratio, ϵ_c , for the NOB model can be expressed using Eq. (43) and $\int_{wake} \left[\frac{D\Omega^{(b)}}{Dt} \right]_{prod.} dA =$

$$\int_{wake} \left[\frac{D\Omega^{(b)}}{Dt} \right]_{Th.} dA \text{ as}$$

$$\epsilon_c = Fr^2 \left[\frac{h_1(\alpha)}{h_2(\alpha)\cos(\alpha) + h_3(\alpha)\sin(\alpha)} \right]. \quad (45)$$

This is qualitatively very similar to the critical Richardson number expression for the Boussinesq model as given in Ref. 32,

$$Ri_c(\alpha) = \frac{g_1(\alpha)}{g_2(\alpha)\cos(\alpha) + g_3(\alpha)\sin(\alpha)}. \quad (46)$$

Thus it is established that the mechanism of vortex shedding suppression by thermal buoyancy is the same as in small-scale heating regimes or Boussinesq regimes.

V. CONCLUSIONS

The effect of heating on the vortex shedding suppression process for the flow of air ($Pr = 0.71$) past a heated square cylinder subjected to a large-scale heating scenario is investigated numerically at a fixed Reynolds number ($Re = 100$). A compressible flow model with variable transport and thermo-physical properties is used in order to capture the large-scale heating effects at a low Mach number ($M = 0.1$). This is the first attempt to understand the vortex shedding suppression process from heated bluff bodies and its mechanism in the large-scale (non-Boussinesq) heating scenario.

It is known that the Richardson number is the parameter or number which solely controls the vortex shedding suppression process in the case of the small-scale heating scenario or Boussinesq flow regime. It is investigated and established with suitable justification that for the case of the large-scale heating scenario or non-Boussinesq model the vortex shedding suppression is controlled to a large extent by a number which is a combination of two different parameters, i.e., over-heat ratio (ϵ) and Froude number (Fr). This number is called Richardson number for the non-Boussinesq model (Ri^{NB}), defined as $Ri^{NB} = \frac{\epsilon}{Fr^2} \left(\frac{2}{2+\epsilon} \right)$. For small heating, $Ri^{NB} \approx Ri$.

Neutral curves separating steady and unsteady flows are developed for the case of the large scale heating scenario in the parametric space of (Ri^{NB} , ϕ) for fixed $\alpha = 0^\circ$, $Re = 100$, $Pr = 0.71$, and for $Fr = 1.0, 0.707$. For each neutral curve, it is found that with an increase in cylinder inclination, the value of Ri_c^{NB} increases monotonically up to $\phi = 40^\circ$ and then its value decreases slightly for $\phi = 45^\circ$. For low values of ϕ , both neutral curves nearly overlap, indicating that for $\phi < 20^\circ$, the vortex shedding suppression is controlled by a single parameter $Ri^{NB} = \frac{\epsilon}{Fr^2} \left(\frac{2}{2+\epsilon} \right)$. This is because for $\phi < 20^\circ$, the amount of heating required is relatively low so that large scale heating effects do not play a significant role in the vortex shedding suppression process.

The relative importance of physical effects, like variations in density or thermal straining of individual fluid particles, variations in transport properties, and specific heat, in controlling vortex shedding suppression is also identified as heating levels are increased. It is found that the specific heat variations do not contribute significantly in the vortex shedding suppression characteristics. In addition to buoyancy, the variations in molecular transport properties contribute more in the vortex shedding suppression phenomena. Hence it is necessary to account for the effects of variations in molecular transport properties under a large-scale heating scenario in order to accurately capture the vortex shedding suppression phenomena for mixed convective flows past heated bluff

bodies. For large-scale heating, the effects of thermal straining also play a weak but tangible role in the vortex shedding suppression process. These findings are applicable to a range of low Re ($O(100)$) as supported by data obtained at $Re = 130$.

The effect of free-stream orientation on the vortex shedding suppression process is also studied, and the neutral curve (ϵ_c Vs α) separating steady and unsteady flows is identified for the large-scale heating scenario in the parametric space of (ϵ , α). The comparison of this neutral curve with the neutral curve obtained for the Boussinesq scenario is also presented. It is found that the neutral curves for both the models (OB as well as NOB) show a similar trend (non-monotonic trend). It is observed that the vortex shedding suppression does not take place for $\alpha \geq 80^\circ$ even for heating levels as high as $\epsilon = 2.0$. The neutral curves for both OB and NOB models show less deviation from each other for small α ($\alpha \leq 20^\circ$), but for $\alpha > 20^\circ$ there is a significant deviation of critical parameters between both models owing to the large scale heating regime involved for $\alpha > 20^\circ$.

The vortex shedding suppression mechanism for the case of the large-scale heating scenario has been investigated using the approach followed in Ref. 32. Analyzing the vorticity dynamics in the wake involving vorticity, density, and dilatation rate variations across the interface of counter-rotating vortices for vortex shedding suppressed states, the role of baroclinic vorticity in the suppression of vortex shedding (as identified in Ref. 32) is extended to the large-scale heating scenario. In addition to the baroclinic effects, the suppression is also shown to be aided by effects of (i) temperature dependence of molecular transport properties and (ii) vorticity production by thermal staining.

ACKNOWLEDGMENTS

The authors acknowledge the computational facilities provided by the Computational and Experimental Heat Transfer Research Laboratory (Mechanical Engineering Department, ZHCET, AMU, Aligarh, India) which was established by the funds provided by DST-PURSE, New Delhi. One of the authors, Md. Reyaz Arif, also acknowledges the UGC, New Delhi, for providing scholarship under the Maulana Azad National Fellowship (MANF) scheme. The authors thank the respected editors and reviewers for giving valuable comments and suggestions which substantially improved the quality of the article.

APPENDIX A: GOVERNING EQUATIONS

1. Generalized coordinates

The governing equations are transformed from rectangular coordinates (x, y) to the body-fitted curvilinear coordinates (ξ, η), where $\xi = \xi(x, y)$ and $\eta = \eta(x, y)$. The system of Eq. (1) in body-fitted coordinates is written as

$$\frac{\partial \mathbf{U}}{\partial t} + \frac{\partial \tilde{\mathbf{F}}}{\partial \xi} + \frac{\partial \tilde{\mathbf{G}}}{\partial \eta} = \tilde{\mathbf{J}}, \quad (\text{A1})$$

where

$$\tilde{\mathbf{F}} = \xi_x \mathbf{F} + \xi_y \mathbf{G}, \quad \tilde{\mathbf{G}} = \eta_x \mathbf{F} + \eta_y \mathbf{G} \quad (\text{A2})$$

and

$$\tilde{\mathbf{J}} = \mathbf{J} + \left(\frac{\partial \xi_x}{\partial \xi} + \frac{\partial \eta_x}{\partial \eta} \right) \mathbf{F} + \left(\frac{\partial \xi_y}{\partial \xi} + \frac{\partial \eta_y}{\partial \eta} \right) \mathbf{G}. \quad (\text{A3})$$

2. Boundary and initial conditions

At the cylinder surface, the conditions of no-slip and no-penetration are applied for the velocity. This may be expressed mathematically in dimensionless form by

$$u = v = 0. \quad (\text{A4})$$

The cylinder surface temperature is maintained constant at an elevated level in comparison to the free-stream temperature. This is given as

$$T = T_w = 1 + \epsilon, \quad (\text{A5})$$

where ϵ is defined as the over-heat ratio given by $\epsilon = (T_w - T_\infty)/T_\infty$.

At infinitely large distances, the free-stream conditions would exist and are written mathematically as

$$\vec{V} = \vec{U}_\infty = U_\infty (\sin \alpha \vec{i} + \cos \alpha \vec{j}), \quad T = 1.0, \quad \rho = 1.0. \quad (\text{A6})$$

In the entire flow field, the undisturbed free-stream conditions are taken as the initial conditions.

APPENDIX B: DIMENSIONLESS OUTPUT PARAMETERS

1. Lift and drag coefficients

The lift and drag coefficients are given by

$$C_L = C_y \sin \alpha - C_x \cos \alpha, \quad C_D = C_x \sin \alpha + C_y \cos \alpha, \quad (\text{B1})$$

where the terms C_x and C_y are the x and y components of the force-coefficients, respectively, given by

$$C_x = \frac{2F_x}{\rho_\infty U_\infty^2 d}, \quad C_y = \frac{2F_y}{\rho_\infty U_\infty^2 d}. \quad (\text{B2})$$

The x and y components of the forces per unit span of the cylinder are denoted as F_x and F_y , respectively. These force coefficients can be written employing the stress distribution²⁴ as

$$C_x = \int_0^1 \frac{2}{|\tilde{\mathbf{J}}|} \left(-p + \frac{4}{3Re} \mu \nabla \cdot \vec{V} \right) \eta_x d\xi - \frac{2}{Re} \int_0^1 \frac{1}{|\tilde{\mathbf{J}}|} \mu \Omega \eta_y d\xi, \quad (\text{B3})$$

$$C_y = \int_0^1 \frac{2}{|\tilde{\mathbf{J}}|} \left(-p + \frac{4}{3Re} \mu \nabla \cdot \vec{V} \right) \eta_y d\xi + \frac{2}{Re} \int_0^1 \frac{1}{|\tilde{\mathbf{J}}|} \mu \Omega \eta_x d\xi. \quad (\text{B4})$$

In the above expression, the quantity Ω is the surface vorticity and $\tilde{\mathbf{J}}$ is the Jacobian defined as

$$\tilde{\mathbf{J}} = \xi_x \eta_y - \xi_y \eta_x. \quad (\text{B5})$$

The integrands in Eqs. (B3) and (B4) are considered at $\eta = 0$ (surface of the cylinder).

2. Nusselt number

The heat transfer from a heated square cylinder to nearby fluid is expressed as a dimensionless number called Nusselt number, which is given by

$$Nu_w = \frac{hd}{\bar{k}_w} = \frac{\bar{Q}}{4\bar{k}_w(T_w - T_\infty)}, \quad (B6)$$

where the term \bar{Q} is defined by the rate of heat transfer per unit span of the square cylinder and is mathematically written as

$$\bar{Q} = - \oint \bar{k}_w (\nabla \bar{T} \cdot \hat{n})_w (d\bar{l}). \quad (B7)$$

In Eq. (B7), the term $d\bar{l}$ is the differential element across the surface of the cylinder, while \hat{n} represents local outward normal to the cylinder boundary. The over-bar represents dimensional quantities. The Nusselt number as defined in Eq. (B6) is transformed into curvilinear coordinates and is given as

$$Nu_w = -\frac{1}{4\epsilon} \int_0^1 \left[\frac{1}{|\bar{j}|} \left(\frac{\partial T}{\partial \eta} \right)_w (\eta_x^2 + \eta_y^2) \right]_{\eta=0} d\xi. \quad (B8)$$

3. Strouhal frequency

For the unsteady flow, the non-dimensional frequency at which the vortex sheds is known as the Strouhal number, which is expressed by

$$St = \frac{fd}{U_\infty}, \quad (B9)$$

where the symbol f denotes the frequency of vortex shedding. The dimensionless frequency or St can generally be recorded by sampling the time history of the lift coefficient (C_L) during the process of vortex shedding, and extracting the time scale of periodic/quasi-periodic oscillations in C_L . This method has been adopted in the present work.

APPENDIX C: NUMERICAL SCHEME

The predictor/corrector steps in a one-dimensional framework are given as⁴²

Predictor step:

$$\mathbf{U}^* = \mathbf{U}^n - \Delta t \left\{ \frac{\mathbf{F}_{i+1/2}^c(\mathbf{U}^n) - \mathbf{F}_{i-1/2}^c(\mathbf{U}^n)}{x_{i+1/2} - x_{i-1/2}} + \frac{\mathbf{F}_{i+1}^{nc}(\mathbf{U}^n) - \mathbf{F}_i^{nc}(\mathbf{U}^n)}{x_{i+1} - x_i} \right\}. \quad (C1)$$

Corrector step:

$$\mathbf{U}^{n+1} = \frac{\mathbf{U}^* + \mathbf{U}^n}{2} - \frac{\Delta t}{2} \left\{ \frac{\mathbf{F}_{i+1/2}^c(\mathbf{U}^*) - \mathbf{F}_{i-1/2}^c(\mathbf{U}^*)}{x_{i+1/2} - x_{i-1/2}} + \frac{\mathbf{F}_i^{nc}(\mathbf{U}^*) - \mathbf{F}_{i-1}^{nc}(\mathbf{U}^*)}{x_i - x_{i-1}} \right\}, \quad (C2)$$

where $i \pm 1/2$ refers to the locations midway on either side of the i th grid node.

This scheme works by splitting the total fluxes into convective flux and non-convective flux as shown in Eqs. (C1) and (C2). The convective flux is expressed by $\mathbf{F}^c = u\mathbf{U}$ and $\mathbf{G}^c = u\mathbf{U}$, while \mathbf{U} is the solution vector as given in Eq. (2). The non-convective fluxes are denoted by \mathbf{F}^{nc} and \mathbf{G}^{nc} , respectively, which are part of the total fluxes excluding the convective fluxes. The estimation of numerical convective and non-convective fluxes is done using different discretization strategies; the detailed description is given in Ref. 42. The numerical convective fluxes are determined at the inter-cell node $i + 1/2$, which is expressed as

$$\mathbf{F}_{i+1/2}^c = u_{i+1/2} \phi_{i+1/2}, \quad (C3)$$

where $u_{i+1/2}$ is the inter-cell particle velocity and $\phi_{i+1/2}$ is the inter-cell convective property vector given by $\phi_{i+1/2} = [\rho \rho u \rho v \rho E]^T$. The inter-cell particle velocity and the inter-cell convective flux vectors are obtained through the blend of higher order central estimates of cubic polynomial and lower order upwind-biased quadratic/linear polynomials through control weight functions. These control weight functions are designed to avoid spurious oscillations in (i) zones of weak convection and/or (ii) a near sudden increase in solution gradients (shocks/discontinuities). For details of the scheme, the work of Hasan et al.⁴² can be seen.

REFERENCES

- C. G. Patel, S. Sarkar, and S. K. Saha, "Mixed convective vertically upward flow past side-by-side square cylinders at incidence," *Int. J. Heat Mass Transfer* **127**, 927–947 (2018).
- R.-J. Yang and L.-M. Fu, "Thermal and flow analysis of a heated electronic component," *Int. J. Heat Mass Transfer* **44**(12), 2261–2275 (2001).
- A. Zebib and Y. K. Wo, "A two-dimensional conjugate heat transfer model for forced air cooling of an electronic device," *J. Electron. Packag.* **111**(1), 41–45 (1989).
- M. R. Rastan, A. Sohankar, and Md. M. Alam, "Low-Reynolds-number flow around a wall-mounted square cylinder: Flow structures and onset of vortex shedding," *Phys. Fluids* **29**(10), 103601 (2017).
- P. A. Irwin, "Bluff body aerodynamics in wind engineering," *J. Wind. Eng. Ind. Aerodyn.* **96**(6–7), 701–712 (2008).
- Md. M. Alam, M. Elhimer, L. Wang, D. Lo Jacono, and C. W. Wong, "Vortex shedding from tandem cylinders," *Exp. Fluids* **59**(3), 60 (2018).
- G. J. Sheard, "Wake stability features behind a square cylinder: Focus on small incidence angles," *J. Fluids Struct.* **27**(5–6), 734–742 (2011).
- Y. Cao and T. Tamura, "Supercritical flows past a square cylinder with rounded corners," *Phys. Fluids* **29**(8), 085110 (2017).
- R. K. Ray and A. Kumar, "Numerical study of shear rate effect on unsteady flow separation from the surface of the square cylinder using structural bifurcation analysis," *Phys. Fluids* **29**(8), 083604 (2017).
- R. F. Huang, C. M. Hsu, and Y. T. Chen, "Modulating flow and aerodynamic characteristics of a square cylinder in crossflow using a rear jet injection," *Phys. Fluids* **29**(1), 015103 (2017).
- A. Sanyal and D. Amit, "Effect of thermal buoyancy on a fluid flowing past a pair of side-by-side square bluff-bodies in a low-Reynolds number flow regime," *Phys. Fluids* **30**(6), 063603 (2018).
- A. Sanyal and D. Amit, "Wake interactions in a fluid flow past a pair of side-by-side square cylinders in presence of mixed convection," *Phys. Fluids* **29**(10), 103602 (2017).
- H. Bai and Md. M. Alam, "Dependence of square cylinder wake on Reynolds number," *Phys. Fluids* **30**(1), 015102 (2018).

- ¹⁴D. Chatterjee, "Triggering vortex shedding by superimposed thermal buoyancy around bluff obstacles in cross-flow at low Reynolds numbers," *Numer. Heat Transfer, Part A* **61**(10), 800–806 (2012).
- ¹⁵H. Jiang and L. Cheng, "Hydrodynamic characteristics of flow past a square cylinder at moderate Reynolds numbers," *Phys. Fluids* **30**(10), 104107 (2018).
- ¹⁶H. Choi, W.-P. Jeon, and J. Kim, "Control of flow over a bluff body," *Annu. Rev. Fluid Mech.* **40**, 113–139 (2008).
- ¹⁷S. Rashidi, M. Hayatdavoodi, and J. Abolfazli Esfahani, "Vortex shedding suppression and wake control: A review," *Ocean Eng.* **126**, 57–80 (2016).
- ¹⁸K.-S. Chang and J.-Y. Sa, "The effect of buoyancy on vortex shedding in the near wake of a circular cylinder," *J. Fluid Mech.* **220**, 253–266 (1990).
- ¹⁹J.-C. Lecordier, L. W. B. Browne, S. L. Masson, F. Dumouchel, and P. Paranthoen, "Control of vortex shedding by thermal effect at low Reynolds numbers," *Exp. Therm. Fluid Sci.* **21**(4), 227–237 (2000).
- ²⁰S. K. Singh, P. K. Panigrahi, and K. Muralidhar, "Effect of buoyancy on the wakes of circular and square cylinders: A schlieren-interferometric study," *Exp. Fluids* **43**(1), 101–123 (2007).
- ²¹A. Rashid and N. Hasan, "Vortex-shedding suppression in mixed convective flow past a heated square cylinder," *Int. J. Mech. Mechatronics Eng.* **5**(6), 88–96 (2011).
- ²²H. Hu and M. M. Koochesfahani, "Thermal effects on the wake of a heated circular cylinder operating in mixed convection regime," *J. Fluid Mech.* **685**, 235–270 (2011).
- ²³M. Darbandi and S. Farid Hosseiniadeh, "Numerical simulation of thermobuoyant flow with large temperature variation," *J. Thermophys. Heat Transfer* **20**(2), 285–296 (2006).
- ²⁴N. Hasan and A. Saeed, "Effects of heating and free-stream orientation in two-dimensional forced convective flow of air past a square cylinder," *Int. J. Therm. Sci.* **112**, 1–30 (2017).
- ²⁵A. Sharma and V. Eswaran, "Effect of aiding and opposing buoyancy on the heat and fluid flow across a square cylinder at $Re = 100$," *Numer. Heat Transfer, Part A* **45**(6), 601–624 (2004).
- ²⁶A. Sharma and V. Eswaran, "Effect of channel-confinement and aiding/opposing buoyancy on the two-dimensional laminar flow and heat transfer across a square cylinder," *Int. J. Heat Mass Transfer* **48**(25–26), 5310–5322 (2005).
- ²⁷A. Sharma and V. Eswaran, "Heat and fluid flow across a square cylinder in the two-dimensional laminar flow regime," *Numer. Heat Transfer, Part A* **45**(3), 247–269 (2004).
- ²⁸S. Bhattacharyya and S. Mahapatra, "Vortex shedding around a heated square cylinder under the influence of buoyancy," *Heat Mass Transfer* **41**(9), 824–833 (2005).
- ²⁹S. Turki, H. Abbassi, and S. Ben Nasrallah, "Two-dimensional laminar fluid flow and heat transfer in a channel with a built-in heated square cylinder," *Int. J. Therm. Sci.* **42**(12), 1105–1113 (2003).
- ³⁰D. Chatterjee and B. Mondal, "Effect of thermal buoyancy on vortex shedding behind a square cylinder in cross flow at low Reynolds numbers," *Int. J. Heat Mass Transfer* **54**(25–26), 5262–5274 (2011).
- ³¹J. P. Dulhani, S. Sarkar, and A. Dalal, "Effect of angle of incidence on mixed convective wake dynamics and heat transfer past a square cylinder in cross flow at $Re = 100$," *Int. J. Heat Mass Transfer* **74**, 319–332 (2014).
- ³²N. Hasan and R. Ali, "Vortex-shedding suppression in two-dimensional mixed convective flows past circular and square cylinders," *Phys. Fluids* **25**(5), 053603 (2013).
- ³³M. Rahnama and H. Hadi-Moghaddam, "Numerical investigation of convective heat transfer in unsteady laminar flow over a square cylinder in a channel," *Heat Transfer Eng.* **26**(10), 21–29 (2005).
- ³⁴R. Ram, A. Dalal, and G. Biswas, "A numerical study of fluid flow and heat transfer around a square cylinder at incidence using unstructured grids," *Numer. Heat Transfer, Part A* **54**(9), 890–913 (2008).
- ³⁵T. Ambreen and M.-H. Kim, "Flow and heat transfer characteristics over a square cylinder with corner modifications," *Int. J. Heat Mass Transfer* **117**, 50–57 (2018).
- ³⁶A. A. Kakade, S. K. Singh, P. K. Panigrahi, and K. Muralidhar, "Schlieren investigation of the square cylinder wake: Joint influence of buoyancy and orientation," *Phys. Fluids* **22**(5), 054107 (2010).
- ³⁷M. Sabanca and F. Durst, "Flows past a tiny circular cylinder at high temperature ratios and slight compressible effects on the vortex shedding," *Phys. Fluids* **15**(7), 1821–1829 (2003).
- ³⁸J.-M. Shi, D. Gerlach, M. Breuer, G. Biswas, and F. Durst, "Heating effect on steady and unsteady horizontal laminar flow of air past a circular cylinder," *Phys. Fluids* **16**(12), 4331–4345 (2004).
- ³⁹P. S. Ghoshdastidar, *Heat Transfer* (Oxford University Press, 2012).
- ⁴⁰C. Hirsch, *Numerical Computation of Internal and External Flows: The Fundamentals of Computational Fluid Dynamics* (Butterworth-Heinemann, 2007).
- ⁴¹J. F. Thompson, Z. U. A. Warsi, and C. W. Mastin, *Numerical Grid Generation: Foundations and Applications* (North-Holland, Amsterdam, 1985), Vol. 45.
- ⁴²N. Hasan, S. M. Khan, and F. Shameem, "A new flux-based scheme for compressible flows," *Comput. Fluids* **119**, 58–86 (2015).
- ⁴³A. Qamar, N. Hasan, and S. Sanghi, "New scheme for the computation of compressible flows," *AIAA J.* **44**(5), 1025–1039 (2006).
- ⁴⁴N. Sharma, A. K. Dhiman, and S. Kumar, "Mixed convection flow and heat transfer across a square cylinder under the influence of aiding buoyancy at low Reynolds numbers," *Int. J. Heat Mass Transfer* **55**(9–10), 2601–2614 (2012).
- ⁴⁵D. Chatterjee and B. Mondal, "Effect of thermal buoyancy on the two-dimensional upward flow and heat transfer around a square cylinder," *Heat Transfer Eng.* **33**(12), 1063–1074 (2012).
- ⁴⁶T. K. Sengupta, K. Venkatasubbaiah, and S. S. Pawar, "Nonlinear instability of mixed convection flow over a horizontal cylinder," *Acta Mech.* **201**(1–4), 197–210 (2008).
- ⁴⁷A. Sohankar, C. Norberg, and L. Davidson, "Low-Reynolds-number flow around a square cylinder at incidence: Study of blockage, onset of vortex shedding and outlet boundary condition," *Int. J. Numer. Methods Fluids* **26**(1), 39–56 (1998).
- ⁴⁸D. Park and K.-S. Yang, "Flow instabilities in the wake of a rounded square cylinder," *J. Fluid Mech.* **793**, 915–932 (2016).
- ⁴⁹K. A. P. Immanuel Paul and S. Vengadesan, "Onset of laminar separation and vortex shedding in flow past unconfined elliptic cylinders," *Phys. Fluids* **26**(2), 023601 (2014).